Sustainable high-pressure light-driven water pump with a spiral tube structure and Büttiker–Landauer ratchet ⊘

Hideyuki Sugioka (杉岡秀行) ✉ ⓘ ; Hiroki Yoshijima (吉嶋大貴) ⓘ

View Online

Export Citation

Sustainable high-pressure light-driven water pump with a spiral tube structure and Büttiker–Landauer ratchet

Hideyuki Sugioka (杉岡秀行),[a] (iD) and Hiroki Yoshijima (吉嶋大貴) (iD)

AFFILIATIONS

Department of Mechanical Systems Engineering, Shinshu University 4-17-1 Wakasato, Nagano 380-8553, Japan

[a]Author to whom correspondence should be addressed: hsugioka@shinshu-u.ac.jp

ABSTRACT

Developing sustainable water transportation technology is essential for solving water shortage problems. In this study, we proposed a sustainable high-pressure light-driven water pump that used a spiral tube structure (where light hit one side and shadowed the other) with a Büttiker–Landauer (BL) ratchet. Moreover, we examined the performance of this water pump. By using a polyurethane tube with a diameter of 2.5 mm and a length of 5 m, we demonstrated that the light-driven BL pump lifted water from a water source against the force of gravity, transported it horizontally along the spiral tube, and removed it from the tube against the surface tension. In particular, by the height scale-up design, we observed $\sim$800 times larger actual pressure difference ($\Delta P \sim 40$ Pa) than the previous light-driven BL pump along with the pumping flow velocity up to 2.4 mm/s. In addition, by proposing a model that considers the effect of the transportation of heat energy from the hot region to the cold region, we explain the experimentally observed self-adjustment phenomenon for a flow velocity. Since our pump can work under sunlight without using electricity or fossil fuels, it is more sustainable than other pumps. Our findings should contribute to practical sustainable water transportation.

Published under an exclusive license by AIP Publishing. https://doi.org/10.1063/5.0121728

I. INTRODUCTION

Water shortages are a serious concern worldwide because they directly affect human health and food problems.[1–3] In addition, global warming and energy shortage have forced us to use renewable energy or sustainable technologies to solve these problems. In this context, one solution is water harvesting technology (fog collection technology) that produces water from moisture in the air[4–7]). The use of this technology can prevent water transportation problems. Another solution is water purification technology, which produces drinking water from non-drinking water such as seawater. A significant amount of non-drinking water can be utilized for other purposes. For example, solar thermal vaporization[8,9] and reverse osmosis membrane[10] technologies for desalination are attractive in coastal areas, and some are at a practical application levels. Moreover, an advanced water sterilization technology[11] that converts toxic water (or used water) into safe water is also useful for agricultural irrigation in water-polluted or urban areas. However, to produce drinkable water from a desalination plant that uses fossil fuels (or to transport water from a water source to a distant location using a water pump that uses fossil energy) is often a realistic option, even though the use of fossil fuels is costly.[2] This is because the

fog collection rate is significantly low;[4–7] water purification technology often incurs high initial and maintenance costs.[8,9] Advanced water sterilization technology has various problems, such as limited bactericidal ability, easily blocked reactors, and psychological barriers for safety.[11] Therefore, it is important to develop alternative treatment methods.

In particular, developing a sustainable technology that can transport water without using fossil energy is essential because the technology not only delivers water to remote areas suffering from water shortages but may also help to produce water with other technologies. For example, a solar irrigation system, which pumps ground water using an electric motor that uses electricity produced from solar photovoltaic (PV) panels, is attractive for the irrigation of remote rural farms. Furthermore, a solar thermal system that transports water using a heat engine that is driven using solar thermal energy is essential for the effective use of unused energy.[3] However, these are not a final solution because of their high installation and maintenance costs.[2] Therefore, we need to explore more innovative technology to solve the water transportation problem. In particular, a water transportation technology that produces a net flow directly from sunlight, without using electricity or fossil fuels has not been explored well.

However, a fundamental issue is the thermal convection phenomenon observed in sustainable fluid transportation, which leads to fluid motion. For example, the flow of the atmosphere and ocean are driven by thermal convection owing to sunlight radiation. Many fundamental studies have been devoted to this issue from the fluid physics perspective.[12–18] For example, Bouillaut *et al.*[13] experimentally demonstrated that the transition from the standard Rayleigh–Bénard (RB) convection (where $Nu \sim Ra^{1/3}$) to the ultimate regimes (where $Nu \propto Ra^{1/2}$) occurred using strong irradiation of metal halide light (where Nu is the Nusselt number and Ra is the Rayleigh number). In detail, Ra is defined as $Ra \equiv \frac{\gamma g \langle \Delta T \rangle h^3}{\nu a}$, where γ is the coefficient of thermal expansion, g is the gravitational acceleration, ν is the kinematic viscosity, a is the thermal diffusivity, and $\langle \Delta T \rangle$ is a time averaged temperature difference between the cold and hot regions of an irradiated liquid chamber of height h. Wang *et al.*[14] theoretically demonstrated that the mean aspect ratio $\Gamma_r \equiv \Gamma/n$ determined the corresponding transport properties of the heat and fluid velocity (Nu and Re) based on numerical simulations, where $Re \equiv \frac{U'H}{\nu}$ is the Reynolds number, n is the number of convection rolls, U' is the time and volume-averaged velocity, $\Gamma = L/H$ is the aspect ratio of the fluid cell, and L and H were the horizontal and vertical lengths of the RB convection system, respectively. Yang *et al.*[15] theoretically demonstrated that time-periodic modulation of frequency f in the temperature boundary condition significantly enhanced the heat flux (Nu) and flow velocity (Re). Here, the selection of the representative length h for the Reynolds number ($Re \equiv \frac{U'h}{\nu}$) is irrelevant to their argument because they presented the behavior of $\frac{Re(f)}{Re(f=0)}$. Note that Ra is the dimensionless temperature difference, while Nu and Re indicate the dimensionless heat transport and flow strength, respectively.[14]

One aspect of the aforementioned thermal convection studies[12–21] clarified the heat and fluid transportation properties of closed systems in which fluids circulated owing to buoyancy forces between hot and cold regions. Here, flow velocity affects the heat flux, whereas heat flux affects the buoyancy force. Consequently, the heat and fluid transportation properties are determined using this adjustment. However, the study of open-loop systems in which the circulated motion of the fluid is transmitted to the next circulation has not yet been explored. This is despite their importance of possibly creating a method to use thermal convection flow to transport fluids to distant locations. In particular, the transport properties of convection flow driven by buoyancy forces in an open spiral-tube structure (which is heated one half by light and shadowed the other) have not been explored yet. Here, the open loop system driven by buoyancy forces shows a periodic temperature distribution that changes between the hot T_h and cold temperatures T_c.

In this context, we previously reported that a thermally driven or light-driven pump using a Büttiker–Landauer (BL) ratchet produced a net circular flow (~0.8 mm/s for the thermally driven BL pump with guide walls,[22] ~0.45 mm/s for the thermally driven BL pump without guide walls,[23] and ~0.27 mm/s for the light-driven BL pump[24]). The BL ratchet is a type of heat engine that produces mechanical work from a periodic temperature in a non-equilibrium state.[25] However, it has not yet been proven that a light-driven BL pump can lift water from a water source against the force of gravity, transport it horizontally, and remove it from the tube against surface tension. Therefore, in this study, we propose a spiral-type light-driven water pump using

a BL ratchet with a spiral tube structure that may significantly increase the pumping pressure and demonstrate the feasibility of the pump.

II. METHOD

A. The basic configuration of the spiral BL light-driven pump

Figure 1 shows the experimental setup of a spiral-type light-driven pump using a BL ratchet. Specifically, Fig. 1(a) shows the front view of the experimental setup. As shown in Fig. 1(a), we fabricated a spiral-light-driven BL pump by winding a transparent polyurethane tube (Uncell Co.) with a length of $l = 5$ m, an outer diameter of $d_1 = 4.0$ mm, an inner diameter of $d_2 = 2.5$ mm, $N_h = 10$ times in a spiral manner around a rectangular heat insulator (cardboard) with a height of $h_3 = 20$ cm, a width of $W_2 = 30$ cm, and a thickness of $W_3 = 2$ mm. Here, the spiral tube had an inlet part of length $h_4 = 3.4$ cm at the right edge, whereas it had an outlet part of length $h_5 = 1.9$–2.2 cm at the left edge. Furthermore, we set the spiral tube structure such that the distance h_6 between the bottom of the cardboard and surface of the experimental table was 6 cm. Furthermore, a water container (beaker) was set below the inlet. Moreover, we defined the water level difference Δh as $\Delta h \equiv h_2 - h_1$, where h_1 was the water level of the water container and h_2 was the level at the edge of the outlet, as shown in Fig. 1(a). Note that we set the initial h_1 such that $h_1 = h_2$ and $\Delta h = 0$ when starting our experiments. Figure 1(b) shows a side view of the experimental setup. As shown in Fig. 1(b), the spiral structure consisted of an oval loop structure with a height of 20.8 cm and a depth of 11.2 cm. Furthermore, we placed two ref-type incandescent light bulbs (Elpa Co., ERF110V 100 W-L) at the center position of the spiral structure so that the distance L between the hotter-side surface of the tube was 6 cm and their heights from the table were 21 and 11 cm, where a ref-type light bulb was a light bulb with a mirror reflector to focus light in the front direction.

B. Principle of the spiral BL light-driven pump

By filling this spiral tube with water (tap water left for a day to degas), water was lifted from the water source (water container) against the force of gravity, transported horizontally along the spiral tube, and pushed out from the tube outlet against surface tension under light irradiation of illuminance I_p (irradiation intensity I_p^*). This was because the light of the light bulbs hit one side of the spiral tube structure and shadowed the other. Consequently, a temperature difference between the sunny and shadowed sides occurred, as shown in Fig. 1(b). In other words, using the spiral tube structure, we produced a ten-cycle periodic temperature distribution consisting of higher-temperature parts (sunny parts) of temperature T_h and lower-temperature parts (shadow parts) of temperature T_c. Therefore, we obtained a high pumping pressure owing to the buoyancy force resulting from the mass difference owing to the temperature difference between the sunny and shadowed parts. Therefore, the water was removed from the source. Here, the length of the area irradiated with light was approximately h_3, considering the spread angle of the light bulbs. Thus, by considering the BL pressure theory,[22] we predicted the following form:

$$\Delta P_{\text{theory}} \simeq C_1 \Delta T \beta \rho_0 g h_3 N_h, \tag{1}$$

where ΔP_{theory} is the theoretical pressure difference produced by the BL pump, $\Delta T \equiv T_h - T_c$ is the temperature difference between the
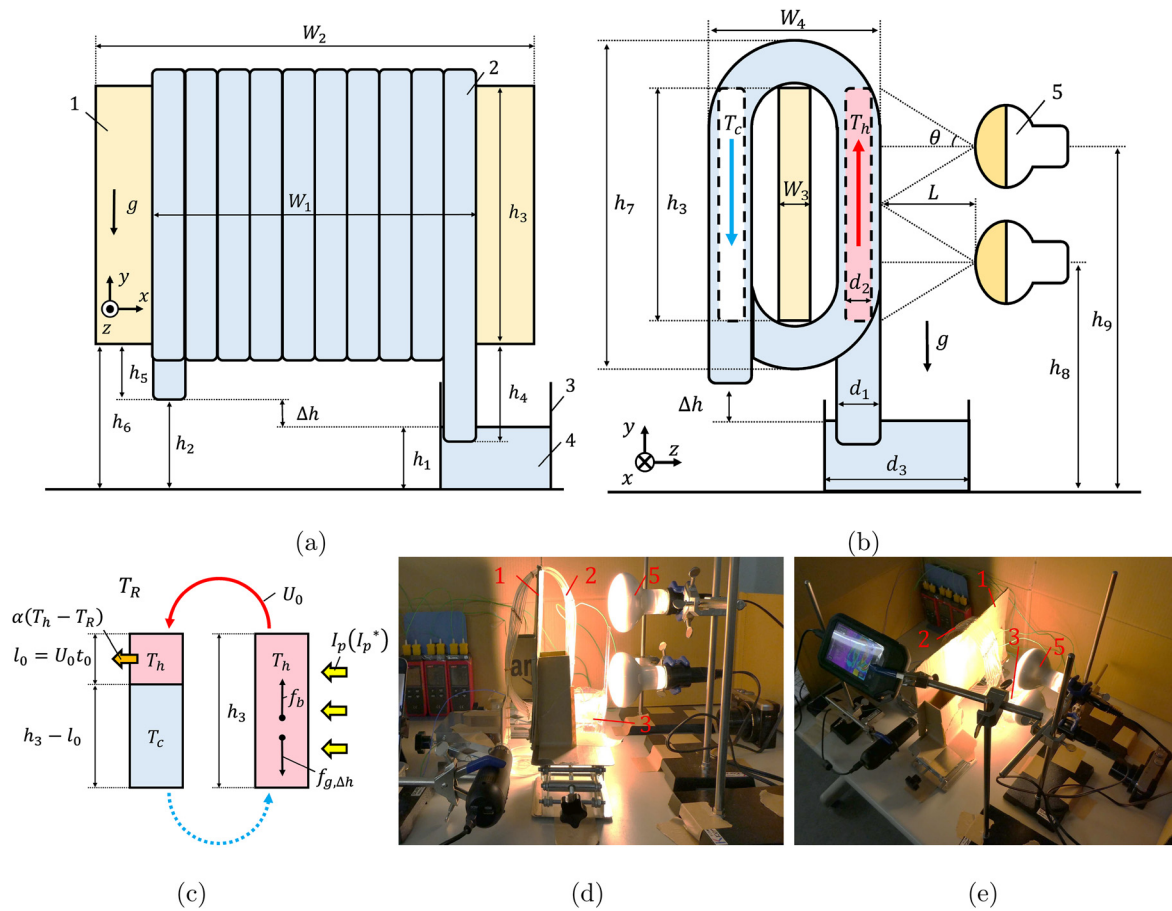
FIG. 1. Schematic view of the spiral light-driven pump using a BL ratchet. (a) Front view. (b) Side view. (c) Heat transportation problem. (d) Photograph (side view). (e) Photograph (bird eye's view). 1: Heat insulating material (cardboard), 2: polyurethane tube of outer d_1 and inner diameters d_2 having a spiral structure, 3: water container (beaker), 4: water (tap water left for a day to degas), and 5: incandescent light bulb. Here, $T_R = 26.0\,°C$, $W_1 = 49$–56 mm, $W_2 = 30$ cm, $W_3 = 2$ mm, $W_4 = 11.2$ cm, $h_2 = 3.8$–4.1 cm, $h_3 = 20$ cm, $h_4 = 3.4$ cm, $h_5 = 1.9$–2.2 cm, $h_6 = 6.0$ cm, $h_7 = 20.8$ cm, $h_8 = 11$ cm, $h_9 = 21$ cm, $L = 6$ cm, $\theta = 40°$, $d_1 = 4.0$ mm, $d_2 = 2.5$ mm, and $d_3 = 6.6$ cm.

sunny and shadow sides, $\beta = -\frac{1}{\rho}\frac{\partial\rho}{\partial T} = 0.38 \times 10^{-3}$ 1/K is the thermal expansion of water at $40\,°C$, $\rho_0 = 992.3$ kg/m^3 is the density of water at $40\,°C$, $g = 9.8$ m/s^2 is the gravitational acceleration, and $C_1 \sim 1$ is a parameter owing to the geometrical condition. However, as shown in Fig. 1(c), part of the heat on the sunny side was transported to the shaded side, which could reduce the pumping performance. Thus, we discussed this heat transportation problem later with our experimental results and elucidated the design concept.

C. Detailed measurement method

Figures 1(d) and 1(e) show the photographs of the experimental system. As shown in these figures, by irradiating the spiral tube with the light bulbs of $I_P = 37\,300$ lx (which corresponded to $I_P^* = 37\,300/250 = 149.2$ W/m^2 [26]) for 55 min (3300 s), we measured the cumulative number of droplets dropped N_d from the outlet, time interval $T_d = 1/f_d$ between the drops, Δh, and temperatures ($T_{h,e}$, $T_{c,e}$, $T_{h,c}$, $T_{c,c}$) of the sunny and shadowed sides at each time t at room temperature $T_R = 26.0°$ C. Here, $T_{h,e}$ and $T_{c,e}$ ($T_{h,c}$ and $T_{c,c}$) were the temperatures measured with thermocouples at the sunny and shadowed sides of the

spiral tube, respectively, at the right edge position (at the center position), whereas we defined the following: $\Delta T_e \equiv T_{h,e} - T_{c,e}$, $\Delta T_c \equiv T_{h,c} - T_{c,c}$, and $\Delta T_a(t) \equiv \frac{1}{2}(\Delta T_c(t) + \Delta T_e(t))$. Furthermore, the illuminance I_e of the ambient light was 37 lx ($\ll I_p$); therefore, we neglected this effect. We observed the falling motion of the droplet around the outlet region with a digital microscope (Sato Shouji Inc., J-scope MJ-ICT16; data size of 640×480 with a frame rate of 30 fps). The temperature distributions of the left-side region of the spiral tube were measured using thermography (FLIR Co., FLIR C5, video data size 640×480 pixels, and detector size 160×120 pixels with a frame rate of 10.38 fps). In addition, after each part was sufficiently cooled to room temperature, we repeated the same measurements, where N ($=1$ or 2) was the trial number.

D. Analysis method

We obtained the volume flow rate $Q(t)$ and average flow velocity $U(t)$ as $Q(t) = \frac{d(\delta V N_d)}{dt} \simeq \delta V/T_d \simeq \delta V f_d$ and $U(t) = Q(t)/S_0$, where $S_0 = \pi d_2^2/4 = 4.91$ mm^2 was the inner cross-sectional area of the

spiral tube and $\delta V = \frac{1}{N_d(t_{\text{final}})}\pi(\frac{d_3}{2})^2 \Delta h(t_{\text{final}})$ (=69.09 and 72.65 mm^3 for $N = 1$ and 2, respectively) was the average volume of the droplet, and t_{final} (= 3310.6 and 3301.3 s for $N = 1$ and 2, respectively) was the final time that the last droplet dropped. Furthermore, we obtained the pressure difference $\Delta P(t)$ experimentally as $\Delta P(t) = R_c Q(t)$, where $R_c(t) = \frac{8\mu l}{\pi(\frac{d_2}{2})^4} = 3.46$ Pa s/mm^3 was a flow resistance considering the Hagen–Poiseuille flow, and $\mu = 0.663$ Pa s was the viscosity of water at 40 °C.

III. RESULTS

A. Observation result for the outlet region

Figure 2 shows the observation results for the outlet region of the spiral BL pump at $N = 2$ when suddenly irradiated with light of $I_p = 37\,300$ lx at $t = 0$ s. Specifically, Figs. 2(a)–2(d) show photographs of the outlet region at $t = 0$, 70.0, 86.0, and 86.8 s, respectively. As shown in these figures, under light irradiation, the water droplet began to grow at the outlet of the tube and dropped out. In other words, using the spiral BL pump, we were able to elevate water from the water container against the force of gravity and succeeded in removing water against surface tension under light irradiation. We discuss the surface tension problem around the outlet region [Fig. 2(c)] in Sec. IV B.

B. Time evolution of the temperature distribution of the spiral BL pump

Figure 3 shows the time evolution of the temperature distribution of the spiral BL pump at $N = 2$. As shown in Fig. 3(a), the temperature difference $\Delta T \equiv T_h - T_c$ between the sunny (right) and shadow (left) tube parts was initially very low [i.e., $\Delta T < 1$ K at $t = 0$ s] because the air temperature is approximately constants. However, by the irradiation

(a)　　　　　　　　(b)
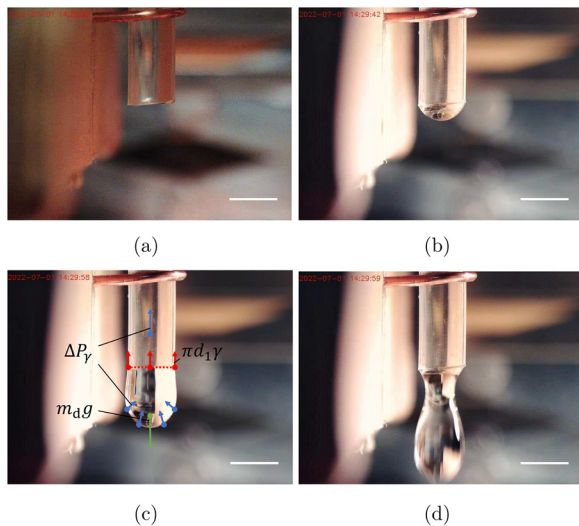
(c)　　　　　　　　(d)

FIG. 2. Observation results of the outlet of the spiral BL pump: (a) $t = 0$, (b) $t = 70.0$, (c) $t = 86.0$, and (d) $t = 86.8$ s. Using the irradiation of light, the water droplet started to grow at the outlet of the tube and dropped out, i.e., we were able to elevate water from the water container against the force of gravity and succeeded in removing it against surface tension. Here, $N = 2$, $I = 37\,300$ lx ($I_p^* = 149.2$ W/m^2), $I_e = 37$ lx, and $T_R = 26.0$ °C; the size of the scale bar is 4 mm.

of the light of $I_p^* = 149.2$ W/m^2, the temperature T_h of the right-side tube increased rapidly. As a result, as shown in Fig. 3(b), we observed the significant temperature difference ($\Delta T \sim 10$ K) at time $t = 87.0$ s, which was the time immediately after the first drop of water. Furthermore, since the significant temperature difference produces a buoyancy force in the fluid of the right-side tube, the fluid in the spiral tube started to move in the anticlockwise direction. Consequently, the heat energy in the right region started to move in the anticlockwise direction. Thus, we observed that the area of the high-temperature region (red region) extended to the upper center tube part at $t = 144.0$ s [Fig. 3(c)], while the temperature T_c of the left-side tube increased to some extent at $t = 300.0$ s [Fig. 3(d)]. However, since there is no light irradiation in the left area, thermal energy escapes into the air during the transportation in the left region. As a result, the temperature distribution becomes steady state. Thus, we observed that the temperature below the left tube increased slightly at $t = 462.0$ s in Fig. 3(e), while the temperature distribution continued until $t = 3300.0$ s [as shown in Fig. 3(f)]. That is, the temperature distribution reached a steady state at $t = 462.0$ s.

C. Time evolution of the parameters

Figure 4 shows the time evolution of these parameters. Specifically, Figs. 4(a) and 4(b) show the dependence of N_d and Δh on t, respectively. As shown in Figs. 4(a) and 4(b), we found that N_d and $\Delta h \sim N_d \delta V / \pi(\frac{d_3}{2})^2$ increased almost linearly (with rates $\frac{dN_d}{dt} \sim 250/3300 \sim 0.076$ drops/s and $\frac{d\Delta h}{dt} \sim 5/3300 \sim 0.0015$ mm/s), although the slope decreased slightly because of the gravity effect owing to the increase in Δh. Furthermore, because the experimental results at $N = 1$ correlated with those at $N = 2$, we understood that our experimental results were reproducible. Figure 4(c) shows the dependence of T_h and T_c on t, whereas Fig. 4(d) shows the dependence of ΔT on t at $N = 2$. From these figures, we observed that T_h, T_c, and ΔT at the center position were larger than those at the edge position. Furthermore, we found that T_h, T_c, and ΔT increased rapidly until $t \sim 400$–500 s, whereas they remained approximately constant at $500 < t < 3300$ s, although ΔT increased slightly [Fig. 4(d)]. Figure 4(e) shows the dependence of f_d on t, whereas Fig. 4(f) shows the dependence of Q and ΔP on t. Because $Q = \delta V f_d$ and $\Delta P = R_c Q$, the behaviors of f_d, Q, and ΔP were similar. Thus, they had their maximum values at $t \sim 120$ s ($f_d^{\max} \sim 0.18$ Hz, $Q^{\max} \sim 13$ mm^3/s, and $\Delta P^{\max} \sim 45$ Pa, respectively). Here, Q ($= S_0 U$) decreased rapidly in the $120 < t < 500$ s range because the high-speed flow resulted in transportation of heat energy from the sunny to shadowed sides. In fact, we observed that the temperature of the upper part of the shadow-side tube increased in the $120 < t < 500$ s range [as shown in Figs. 3(c)–(e)]. Consequently, the pumping pressure decreased rapidly, and, thus, Q ($= S_0 U$) decreased rapidly such that U and ΔT maintained quasi-steady states. Here, in detail, a slight decrease in U and a slight increase in ΔT occurred at $t > 500$ s owing to the increase in Δh in the quasi-steady state. In other words, f_d, Q, and ΔP were approximately constant ($f_d \sim 0.08$ Hz, $Q \sim 6$ mm^3/s, and $\Delta P \sim 20$ Pa) but decreased slightly with t because of the gravitational force effect $\Delta h S_0 \rho_0 g$. Here, we predicted that they became zero at $t \sim 284$ min using extrapolation.

D. Dependence of f_d, Q, ΔP, and U on Δh

Figures 5(a)–5(d) show the dependence of f_d, Q, ΔP, and U ($= Q/S_0$) on Δh, respectively. From these figures, we found that the
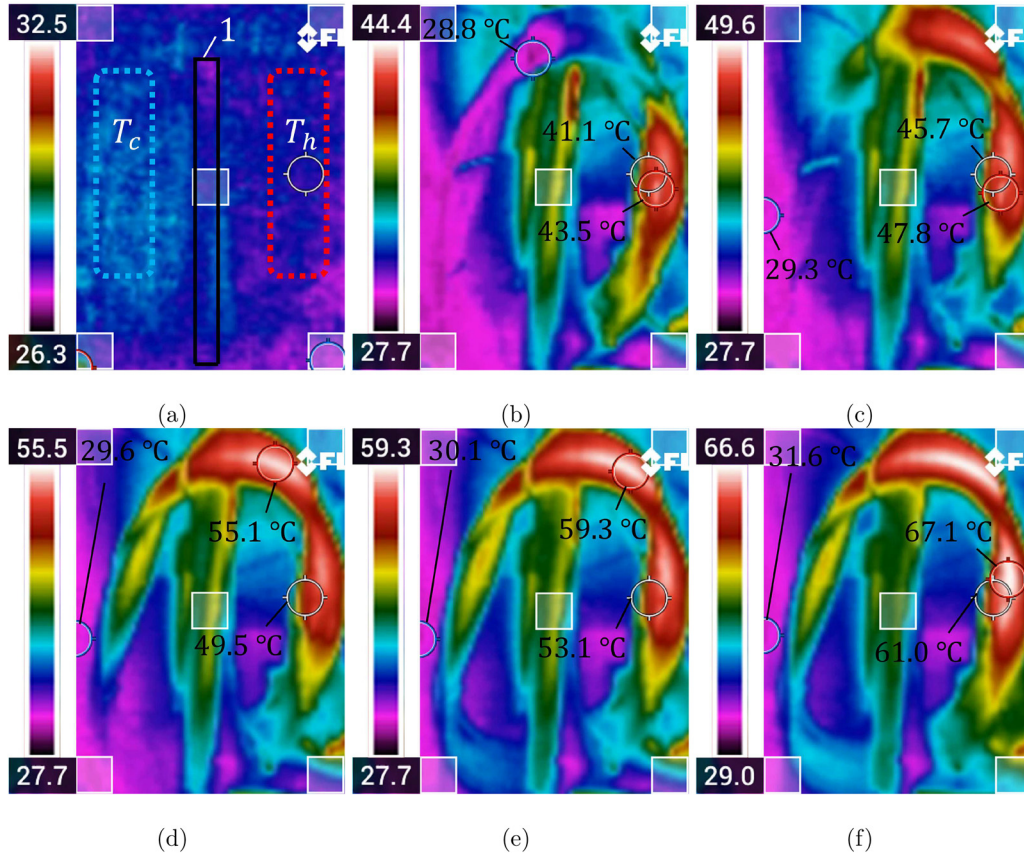
FIG. 3. Time evolution of the temperature distribution of the spiral BL pump: (a) $t = 0$, (b) $t = 87.0$, (c) $t = 144.0$, (d) $t = 300.0$, (e) $t = 462.0$, and (f) $t = 3300.0$ s. Here, $N = 2$, $I = 37\,300$ lx ($I_p^* = 149.2$ W/m^2), $I_e = 37$ lx, and $T_R = 26.0$ °C. Note that the red circle shows the highest temperature region in the measurement area, whereas the blue circle shows the lowest temperature region; the white circle indicates the approximate center of heating but does not represent the exact location; furthermore, the central rectangular area indicates the center of the measurement area and is not related to temperature information.

BL pump elevated water against the force of gravity up to at least $\sim$5 mm. Furthermore, by extrapolating the quasi-steady part in the range of $1 \leq \Delta h \leq 5$ mm, we predict that the pump cannot operate at $\Delta h \sim 17$ mm, as shown in Figs. 5(c) and 5(d). The reason why the pump cannot work approximately at $\Delta h > 17$ mm is that Δh exceeds the critical water level difference Δh_c. Here, the pressure ΔP_g (generated by the gravitational force owing to Δh) is described as $\Delta P_g = \rho_0 \Delta hg$. Thus, the expression $\Delta P_{\text{theory}} = \Delta P_g$ (i.e., $C_1 \Delta T_a \beta \rho_0 g h_3 N_h = \rho_0 \Delta h_c g$) helps determine Δh_c as

$$\Delta h_c \sim \frac{\Delta P_{\text{theory}}}{\rho_0 g} \sim \Delta T \beta h_3 N_h. \qquad (2)$$

Thus, we obtain $\Delta h_c = 16.7$ mm for $\Delta T_a \sim 22$ K. Therefore, we proposed a phenomenological model (model A) to explain our experimental results as $\Delta P_A = \eta(\Delta P_{\text{theory}} - \Delta P_g)$ and, thus, we obtained the following form:

$$U_A = \frac{\eta}{S_0 R_c}(\Delta P_{\text{theory}} - \Delta P_g), \qquad (3)$$

where $\eta = 0.15$ was obtained from the fitting between the experimental and theoretical results. Note that because multiple data points often

corresponded to the same Δh, the mean value and error bar (standard deviation) were shown in Fig. 5.

E. Additional experiment for a long time operation (3 h)

In the previous study,[24] we only demonstrated that the light-driven BL pump works for $\sim$60 s. Thus, Fig. 4 shows that our pump works enough time ($\sim 3500 \gg 60$ s). However, if models A and B (Sec. IV A) are correct, our pump should work even at $\Delta h \sim 10$ mm. Figure 6 shows the additional experiment for a long time operation (3 h) under the same condition as the condition in Figs. 4 and 5. Note that in detail, we used reboiled water for the additional experiments (Figs. 6–8). From Fig. 6, we find that we can operate our device at least 3 h, and the trend of the time evolution of Δh, Q, ΔP, and U is the same as the results in Figs. 4 and 5. In particular, from Fig. 6, we find that at $t = 10\,794$ s ($\sim$3 h), our pump works under the condition that $\Delta h = 12.93$ mm, $Q = 2.56$ mm^3/s, $U = 0.52$ mm/s, and $\Delta P = 8.87$ Pa. Moreover, we find that the large spike noise exists at $t \sim 9500$ s. This is because small bubbles were generated and detached in the tube of the sunny side. Although we were able to operate our pump after the event, the bubble generation in the tube can be an obstacle for the long term operation in
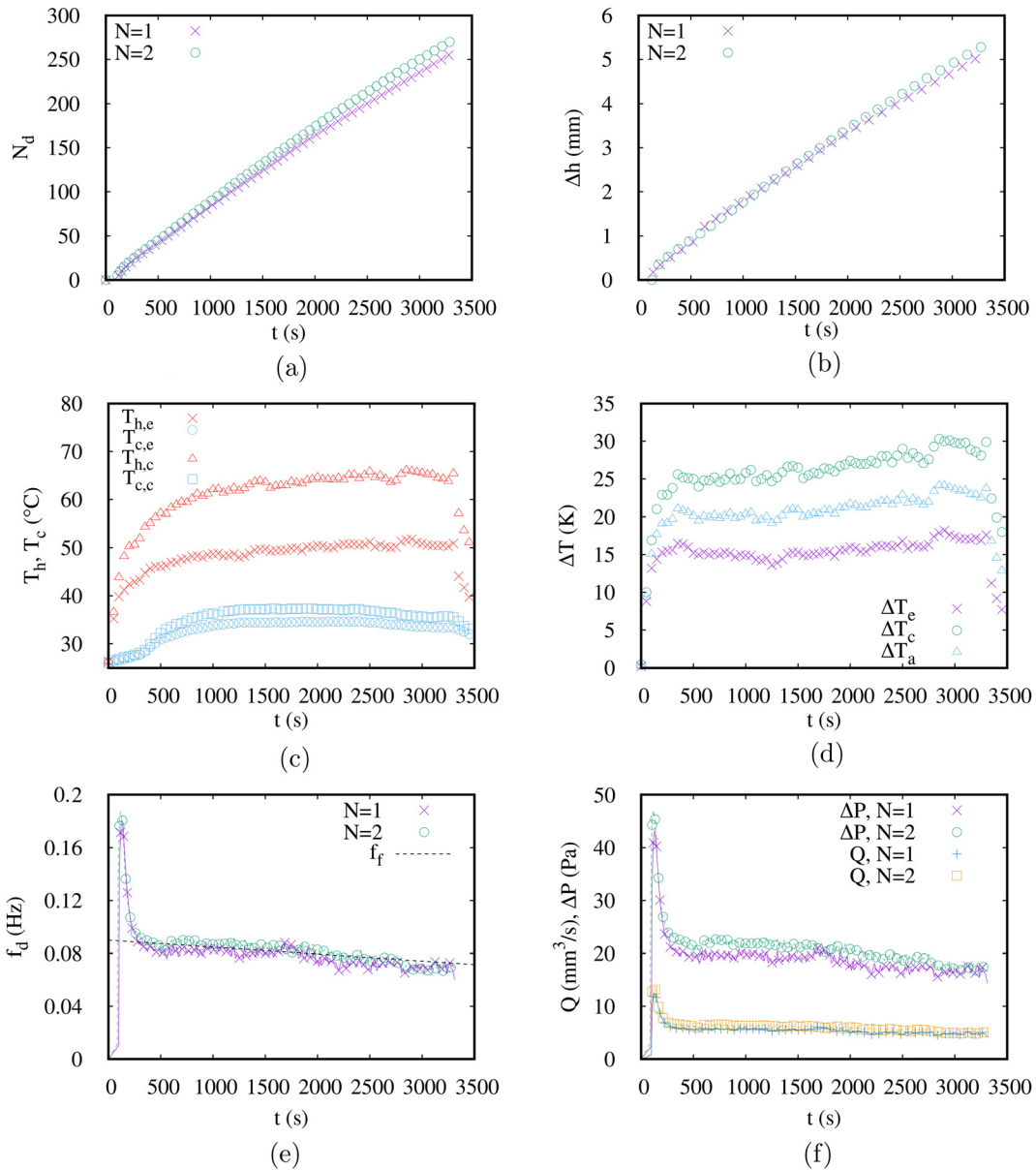
FIG. 4. Dependence of the parameters: (a) N_d vs t, (b) Δh vs t, (c) T_h, T_c vs t ($N=2$), (d) ΔT vs t ($N=2$), and (e) f_d vs t. (f) Q, ΔP vs t. Here, $I=37\,300$ lx ($I_p^* = 149.2$ W/m^2), $I_e = 37$ lx, and $T_R = 26.0\,°$C.

the future. Furthermore, as shown in Figs. 6(c) and 6(d), $Q = S_0 U$ and U decrease approximately as we predicted by model A. However, in detail, the decreasing rate of U becomes small with Δh, and the concept of model A is corrected by model B, which will be explained in Secs. IV A, IV D, and IV F.

F. Additional experiment on the effect of improved heat dissipation

If model B (Sec. IV A) is correct, U and Q should be improved when the heat dissipation time is improved. Figure 7 shows the

additional experiment on the effect of improved heat dissipation. That is, by using a dryer (Tescom co., TID295, the flow rate: $\sim$1.1 m^3/min, exit cross sectional area: $\sim$0.0016 m^2, flow velocity; $\sim$11 m/s), we blew the wind to the top region of the tube from a position 55 mm away from the tube on the shaded side for 60 s periodically with a period 360 s, 3 times. Figure 7(a) shows the temperature distribution just before we blow the wind (at $t=600$ s), whereas Fig. 7(b) shows the temperature distribution just after we blew the wind (at $t=660$ s). As shown in these figures, we find that the upper part of the left (shadow) side can be cooled down by the wind from the dryer. As a result, we

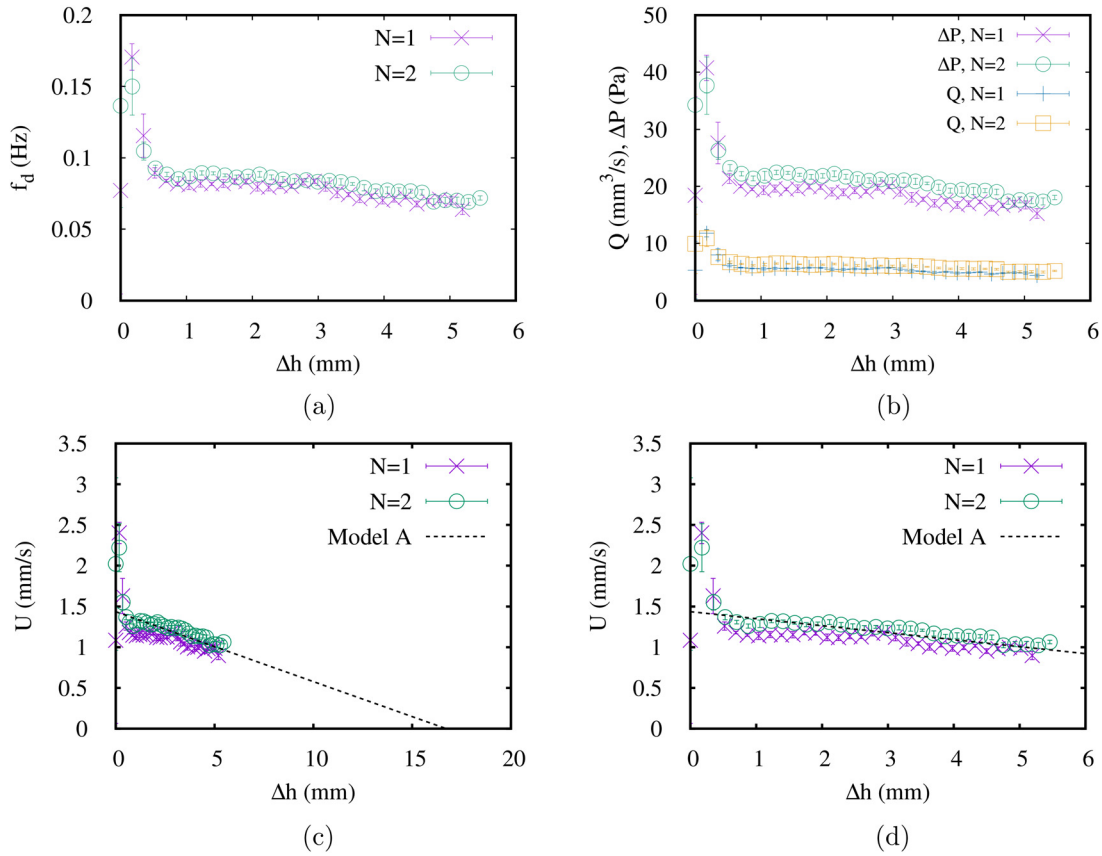**FIG. 5.** Dependence of f_d, Q, ΔP, and U on Δh: (a) f_d vs Δh; (b) Q, ΔP vs Δh; (c) U vs Δh ($0 < \Delta h < 20$ mm); and (d) U vs Δh ($0 < \Delta h < 6$ mm). Here, $I = 37300$ lx ($I_p^* = 149.2$ W/m^2), $I_e = 37$ lx, and $T_R = 26.0\,^\circ$C.

find that Q and ΔP increase periodically by the blow of a wind, which promotes heat dissipation of the shadow side tube, as shown in Fig. 7(c). In Fig. 7(c), the second to fourth peaks show the increasing due to the improvement of dissipation, while the first peak shows the peak due to the auto adjustment mechanism explained before. Furthermore, Fig. 7(d) shows the dependence of Δh on t. In Fig. 7(d), we find that Δh increases due to the periodic blow compared to the control experiment.

G. Additional experiment on the height scale-up problem ($h_3 = 0.4$ m)

If model B (Sec. IV A) is correct, U and Q should be improved significantly when h_3 becomes double, although we often consider that U and Q do not change because both ΔP and R_c also become double. Figure 8 shows the additional experiment on the height scale-up problem under the same condition as that in Figs. 4 and 5, except that $h_3 = 0.4$ m. As shown in Fig. 8(a), the droplet ejection frequency f_d has a peak value ($f_d \simeq 0.3$ Hz) at $t \sim 150$ s and keep a constant value (~ 0.18 Hz) at $t > 400$ s. As a result, ΔP, Q, and U also have peak values ($\Delta P \sim 60$ Pa, $Q \sim 18$ mm^3/s, and $U \sim 3.5$ mm/s) at $t \sim 150$ s and keep constant values ($\Delta P \sim 40$ Pa, $Q \sim 11$ mm^3/s, and $U \sim 2.4$ mm/s) at $t > 400$ s. In other words, U and Q was improved

significantly as predicted by model B. Note that we will discuss in Secs. IV A, IV D, and IV F for model B.

IV. DISCUSSION

A. Model for η (model B)

In Fig. 1(c), the heat energy at the sunny side was transported using the generation of flow velocity U_0 to the shadow side and subsequently dissipated into the air. Thus, by assuming cooling time t_0 and transportation length $l_0 \sim U_0 t_0$, we obtained the balance relation $C_p \rho_0 \pi (\frac{d_2}{2})^2 l_0 \Delta T_a = \alpha \Delta T_{hR} \pi d_1 l_0 t_0$; $t_0 = \frac{\rho_0 C_p d_2}{4\alpha} r_1 r_2$ (118.8 s for $\Delta T_a = 22$ K), where $r_1 = \frac{d_2}{d_1} = 2.5/4 = 0.625$, $r_2 = \frac{\Delta T_a}{\Delta T_{hR}} \sim 22/30 \sim 0.73$, $\Delta T_{hR} \equiv \frac{1}{2}(T_{h,c} + T_{h,e}) - T_R \sim 30$ K, and $C_p = 4.178$ kJ/(kg K) was the specific heat at $40\,^\circ$C, and $\alpha \sim 10$ W/(m^2 K) was the heat transfer coefficient of water. As the cooling part shrunk from h_3 to $h_3 - U_0 t_0$, the ideal flow velocity

$$U^* = \frac{1}{S_0 R_c}(\Delta P_{\text{theory}} - \Delta P_g), \qquad (4)$$

decreased to U_0. Thus, U_0 was described as $U_0 = \frac{h_3 - U_0 t_0}{h_3} U^*$. Therefore, we obtain
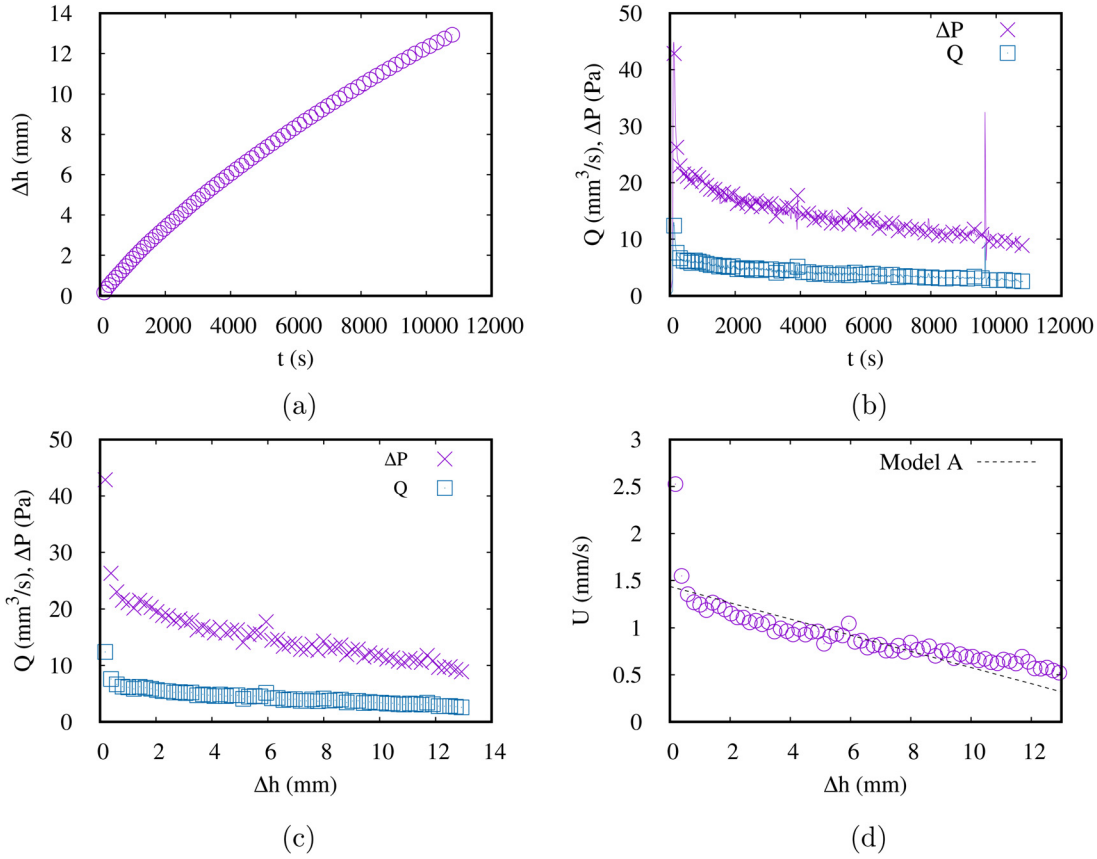
FIG. 6. Additional experiment for the long time operation (3 h): (a) Δh vs t; (b) Q, ΔP vs t; (c) Q, ΔP vs Δh; and (d) U vs Δh. Here, $I = 37\,300$ lx ($I_p^* = 149.2$ W/m^2), $I_e = 37$ lx, and $T_R = 25.8\,^\circ$C.

$$U_0 = \frac{1}{1+G} U^*, \tag{5}$$

$$G \equiv \frac{U^* t_0}{h_3}. \tag{6}$$

Thus, the value of η was predicted to be

$$\eta_B = \frac{1}{1+G} \sim 0.15, \tag{7}$$

with the related parameters ($G = 5.69$, $l_0 = 170.1$ mm, $h_3 - l_0 = 29.9$ mm, and $U_0 = 1.432$ mm/s) for $\Delta T_a \sim 22$ K. That is, we succeeded in explaining the experimental value $\eta_{\text{expt.}} = 0.15$ based on our simple model (model B). Note that $\Delta P_{\text{theory}} \geq \Delta P_g$ should be satisfied to keep $U^* \geq 0$.

B. Pressure owing to droplet surface tension

In the aforementioned models, we did not consider the pressure difference (Laplace pressure) $\Delta P_\gamma \sim 4\frac{\gamma}{d_1}$ ($= 69.4$ Pa at $40\,^\circ$C), owing to the surface tension γ ($= 69.4$ mN/m at $40\,^\circ$C) of the droplet [see Fig. 2(c)]. This is mainly because the BL pump potentially produces a sufficient pressure difference $\Delta P^* \equiv \Delta P_{\text{theory}} - \Delta P_g$ ($= 162.6$ Pa at $\Delta h = 0$ mm) to overcome the Laplace pressure. Moreover, the

generated velocity U_0 is eventually adjusted from the potential velocity U^* corresponding to ΔP^* to $U_0 = \eta U^*$ automatically using the mechanism of model. In other words, although we need to grow droplets against the Laplace pressure $\Delta P_\gamma = 69.4$ Pa, the driving pressure $\Delta P_{\text{theory}} - \Delta P_g - \Delta P_\gamma = 162.6 - 69.4 = 93.2$ Pa is much larger than that of the adjusted apparent pressure $\Delta P_A \sim 20$ Pa; therefore, we can neglect the effect of ΔP_γ. Furthermore, the conditions for separating droplets from the outlet of the tube were as follows: $\pi d_1 \gamma = \delta V_{d,C} \rho_0 g + S_0 \Delta P_A$, where $\delta V_{d,C}$ is the expected volume of the separated droplet. Thus, we obtained $\delta V_{d,C} = (\pi d_1 \gamma - S_0 \Delta P_A)/ (\rho_0 g) \sim 89$ mm^3, which explained the experimental value $\delta V = 69$–72 mm^3 to some extent.

C. Energy efficiency of our device

In Fig. 1(a), the total irradiation energy per unit time on irradiation side is given as $E_{\text{light}} = 10 h_3 d_1 I_p^* = 1.19$ W, whereas the produced kinetic and potential energies are given as $E_k = \frac{1}{2}\dot{m}U^2 \simeq 4.29$ pW and $E_g = \rho_0 \pi (\frac{d_2}{2})^2 \Delta h g U = \dot{m} g \Delta h \simeq 58.3$ nW, respectively for the typical pumping performance (i.e., $U \sim 1.2$ mm/s, $Q \sim 6$ mm^3/s, $\Delta P \sim 20$ Pa, and $\Delta h \sim 1$ mm at $I_p^* = 149.2$ W), where $\dot{m} = \rho_0 Q = 5.95 \times 10^{-6}$ kg/s is a mass flow rate. Thus, if we define
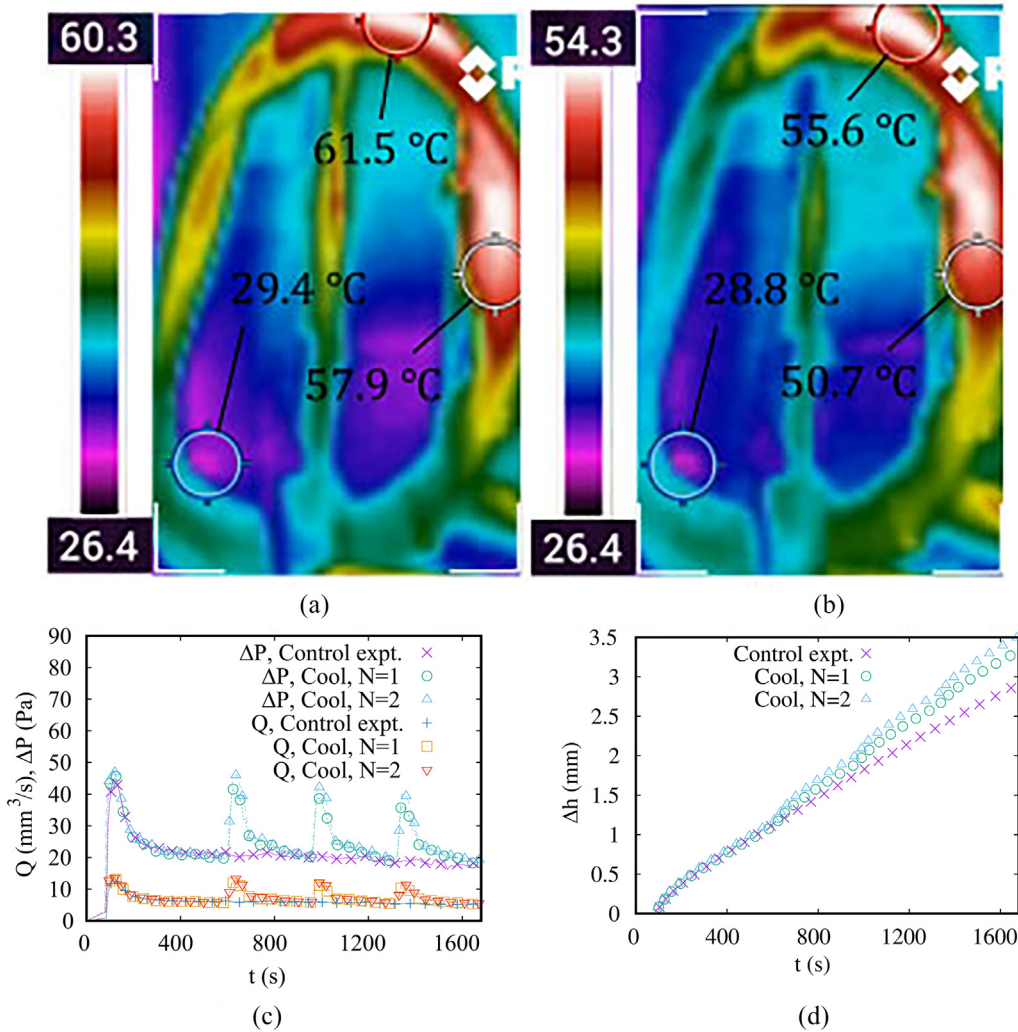
FIG. 7. Additional experiment on the effect of improved heat dissipation: (a) $t = 600$; (b) $t = 660$ s; (c) Q, ΔP vs t; and (d) Δh vs t. In (c), "x" and "+" show the results of the control experiment (which did not use the blow) for ΔP and Q, respectively; In (d), "x" shows the results of the control experiment. Here, $I = 37\,300$ lx ($I_p^* = 149.2$ W/m^2), $I_e = 36$ lx, and $T_R = 25.5$ °C.

the energy efficiency of our pump as $\eta_E \equiv \frac{E_k + E_g}{E_{light}} \sim \frac{E_g}{E_{light}}$, we obtain that $\eta_E \sim 4.89 \times 10^{-8}$ for the typical performance. Furthermore, since the estimated limit of Δh is 17 mm, we can estimate the maximum values of E_g and η_E as $E_g \sim 0.992$ μW ($\gg E_k$) and $\eta_E \sim 8.31 \times 10^{-7}$. Unfortunately, this energy efficiency is very low compared with the conventional water pump, and even compared with the Carnot thermal efficiency $\eta_c \sim 1 - \frac{273.15+26}{273.15+55} \sim 0.09$, which is the limit value due to the second law of thermodynamics when the temperatures of the hot and cold heat sources are 55 and 26 °C, respectively. However, our water pump can be operated without using electricity or fossil fuels and can produce a net flow directly from sunlight. Note that conventional water pumps produce a net flow by using a mechanical power that was produced by electric motors or thermal engines. Usually, energy efficiency of the pump part is approximately 30%–85%, whereas energy efficiency of the motor (engine) part is ~80% (~40%); thus, the total energy efficiency is approximately 12%–68%.

D. Comparison between the experimental results and the results of model B

Figure 9 shows the comparison between the experimental results and the results of model B. Specifically, Figs. 9(a) and 9(b) show the comparison in the range of $0 < \Delta h < 6$ mm. As shown in Figs. 9(a) and 9(b), the experimental values of U and Q approximately keep a constant value, and this trend qualitatively agrees with that of model B, which predicts the self-flow adjustment function originating from the heat transportation from the sunny to shadowed sides (see Secs. III B, III C, and IV A). Furthermore, Figs. 9(c) and 9(d) show the

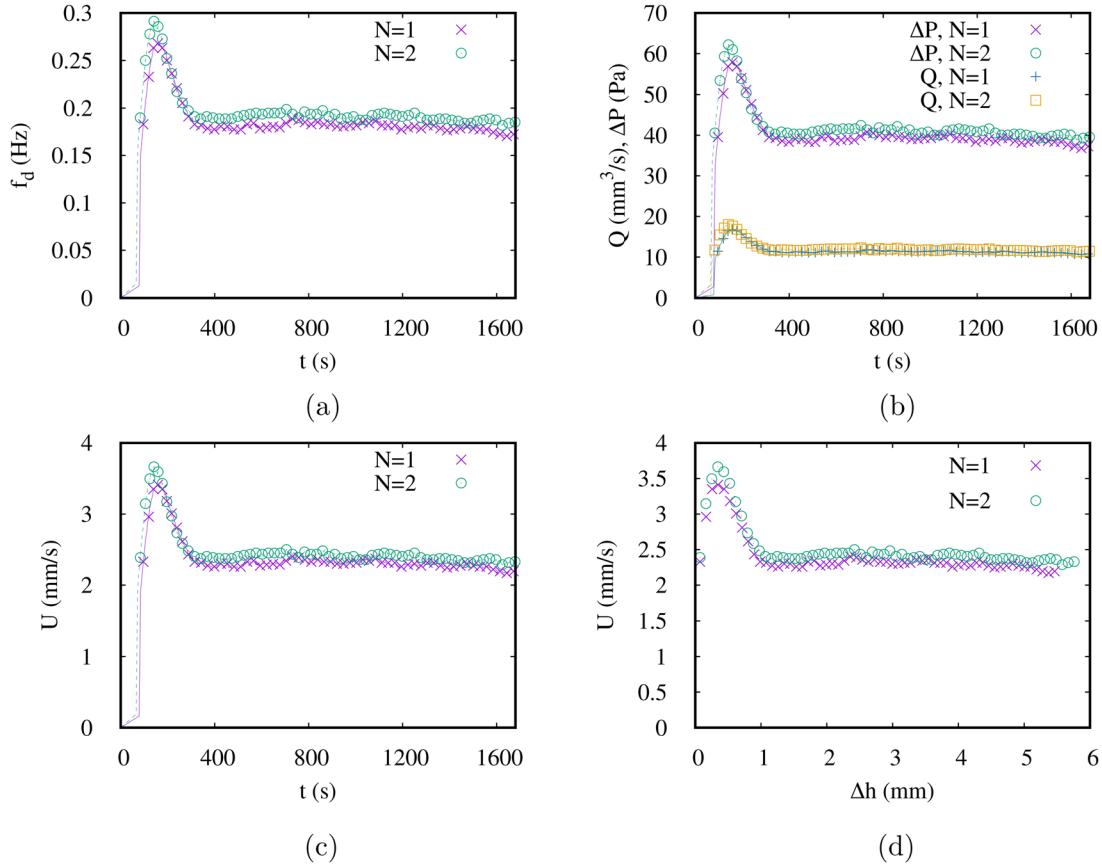**FIG. 8.** Additional experiment on the height scale up problem ($h_3 = 40$ cm): (a) f_d vs t; (b) Q, ΔP vs t; (c) U vs t; and (d) U vs Δh. Here, $I = 37\,300$ lx ($I_p^* = 149.2$ W/m^2), $I_e = 39$ lx, and $T_R = 26.2$ °C.

comparison in the range of $0 < \Delta h < 16$ mm. In these figures, although the experimental values seem to decrease faster with Δh than theoretical predictions, we consider that model B that assumes $\alpha = 10$–5.6 W/m^2 K (i.e., $\alpha \sim 10$ W/m^2 K) explains the experimental results to some extent, because model B explains dynamic change of U and Q at $t \sim 100$ s. Here, we need to take a long time (3 h) to obtain the data for $5 < \Delta h < 14$ mm. Thus, there is a possibility that the local ambient environment related to heat dissipation has changed subtly. Figures 9(e) and 9(f) show the comparison at $h_3 = 0.4$ m. As shown in Figs. 9(e) and 9(f), the constant part of the experimental results agrees with those of model B. Here, we just took ~ 30 min to obtain the data in the range $0 \leq \Delta h \leq 6$ mm because the flow velocity $U \sim 2.4$ mm/s is much larger than that at $h_3 = 0.2$ m. We consider that this is the reason why the experimental and theoretical results agrees with each other.

E. Dependence of U and U^* on ΔT and the relation to the fundamental convection study

Figure 10 shows the dependence of U and U^* on ΔT and the relation to the fundamental convection study. As shown in Fig. 10, U^* increases linearly with ΔT, whereas U increases non-linearly with ΔT.

Here, $U = \eta U^*$. Since $U^* = 0$ at $\Delta T = 0$, $\eta \equiv \frac{1}{1+G} = 1$, and $G \equiv \frac{U^* t_0}{h_3} = 0$ at $\Delta T = 0$. As ΔT increases, η decreases. Thus, we can write U as $U \sim A \Delta T^\beta$ at the interested region of ΔT. For example, we may approximate U as $U \sim 0.55 \Delta T^{1/3}$ in the range of $5 < \Delta T < 25$ K, as shown in Fig. 10(a). Note that similar relation is known for the fundamental study of the thermal convection in a chamber,[13] as mentioned in Sec. I, since $Ra \propto \Delta T$.

F. Scale-up ability

1. Scale-up design of the current device

Previously, we reported that the light-driven BL pump having light-absorbing and reflecting parts of height h_3 ($=1.5$ mm) (the unit number $N_h = 3$ and the channel hydraulic diameter $\phi_h \sim 3$ mm) produces a net flow of ~ 0.27 mm/s (flow rate ~ 10 mm^3/s) under the light irradiation of $I_p^* = 160$ W.[24] Since $\Delta P_{\text{theory}} \propto N_h h_3$ from Eq. (1), we can improve ΔP_{theory} by increasing $N_h h_3$. Therefore, in the current device design, we increased N_h from 3 to 10, while we increased h_3 from 1.5 to 200 mm; i.e., we increase $N_h h_3$ from 4.5 to 2000 mm (Fig. 4). Thus, we expect that ΔP_{theory} intrinsically increases by $2000/4.5 \sim 444$ times. Furthermore, from Eq. (1), ΔP_{theory} is also proportional to ΔT (and I_p^*). Thus, since we here used $I_p^* = 149.2$ W, we
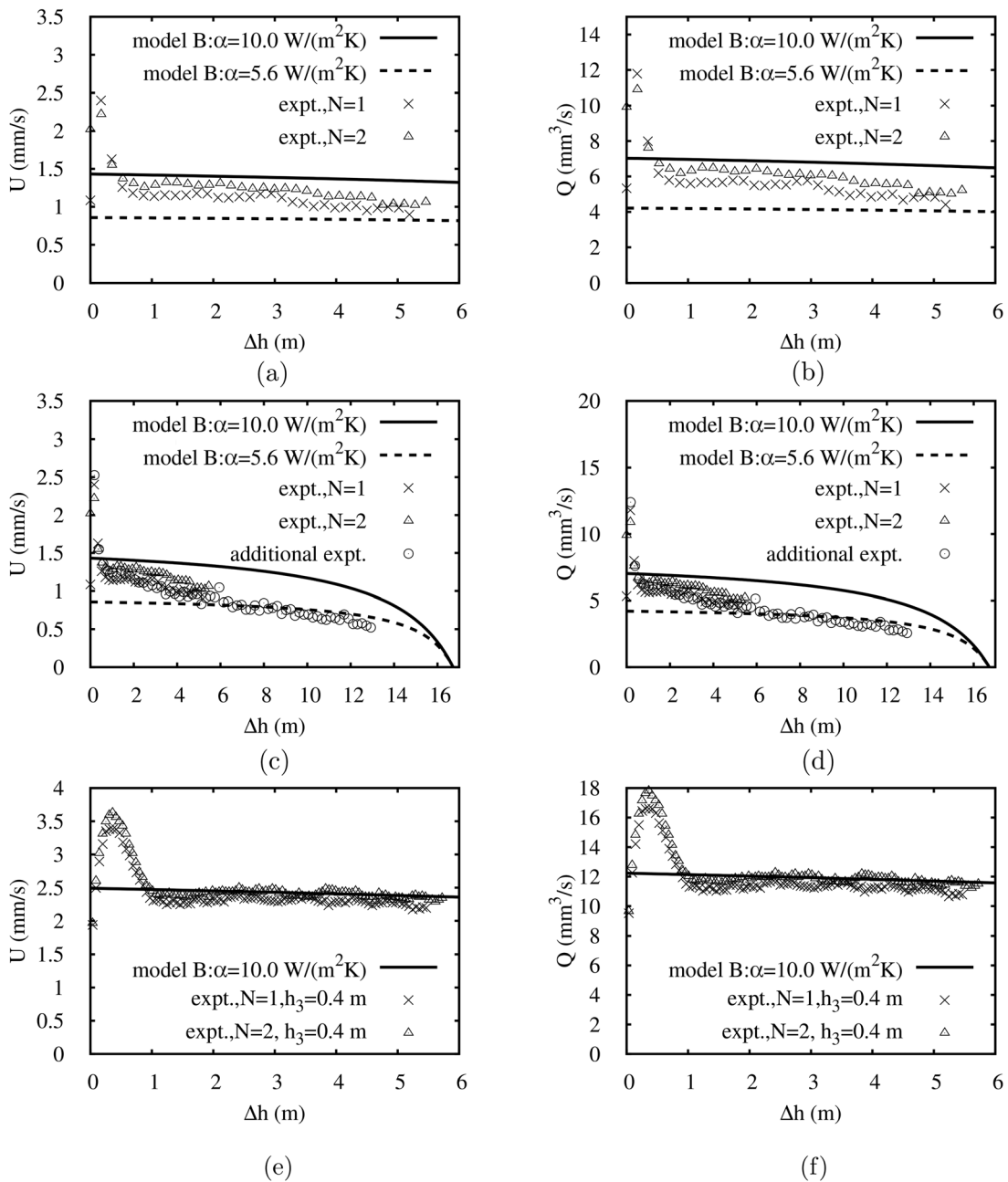
FIG. 9. Comparison between the experimental results and the results of model B: (a) U vs Δh ($0 < \Delta h < 6$ mm, $h_3 = 0.2$ m); (b) Q vs Δh ($0 < \Delta h < 6$ mm, $h_3 = 0.2$ m); (c) U vs Δh ($0 < \Delta h < 16$ mm, $h_3 = 0.2$ m); (d) Q vs Δh ($0 < \Delta h < 16$ mm, $h_3 = 0.2$ m); (e) U vs Δh ($0 < \Delta h < 6$ mm, $h_3 = 0.4$ m); and (f) Q vs Δh ($0 < \Delta h < 6$ mm, $h_3 = 0.4$ m). Here, $I_p^* = 149.2$ W/m^2, $N_h = 10$, $\mu = 0.663$ Pa s, $\beta = 0.38 \times 10^{-3}$ 1/K, $\rho_0 = 992.3$ kg/m^3, $C_p = 4.178$ kJ/(kg K), $C_1 = 1$, $\Delta T = 22$ K, and $d_2 = 2.5$ mm.

expect that ΔP_{theory} of the current BL device is 414 ($\sim 444 \times \frac{149.2}{160}$) times larger than that of the previous device. In fact, the apparent experimental pressure difference ($\Delta P_{\text{expt.}} \sim 20$ Pa) of the current device (Fig. 4) is approximately 400 times larger than that of the previous BL pump ($\Delta P_{\text{expt.}} \sim 0.05$ Pa).[24] In other words, we have

demonstrated the scale-up ability of our BL pump at least for $N_h h_3$, although we need to explore the scale-up problems more in the future, as discussed in the following sessions. In addition, by the additional experiment at $h_3 = 0.4$ m (Fig. 8), we have also demonstrated that the apparent experimental pressure difference ($\Delta P_{\text{expt.}} \sim 40$ Pa) of
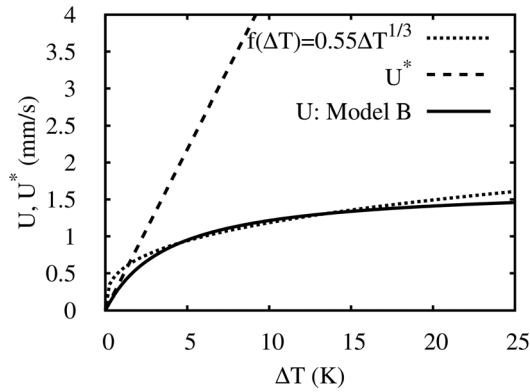
FIG. 10. Dependence of U and U^* on ΔT and the relation to the fundamental convection study. Here, $I_p^* = 149.2$ W/m^2, $N_h = 10$, $h_3 = 0.2$ m, $\mu = 0.663$ Pa s, $\beta = 0.38 \times 10^{-3}$ 1/K, $\rho_0 = 992.3$ kg/m^3, $\alpha = 10$ W/(m^2 K), $C_p = 4.178$ kJ/(kg K), $C_1 = 1$, and $d_2 = 2.5$ mm.

the current device (Fig. 8) is approximately 800 times larger than that of the previous BL pump ($\Delta P_{\text{expt.}} \sim 0.05$ Pa).[24] Furthermore, we have demonstrated that the flow velocity $U_0 \sim 2.4$ mm/s at $h_3 = 0.4$ m (Fig. 8) is approximately 9 times larger than that of the

previous BL pump,[24] while the volume flow rate $Q_0 \sim 11$ mm^3/s at $h_3 = 0.4$ m (Fig. 8) is approximately the same as than that of the previous BL pump.[24]

2. Height scale-up in the future

From Eqs. (1) and (2), we understand that $\Delta P_{\text{theory}} \propto h_3$ and $\Delta h_c \propto h_3$. Thus, in the future, height scale-up of the spiral BL pump will improve Δh_c, which is the ability that how high the pump can raise water. For example, if we increase h_3 from 0.2 to 10 m by using the walls of cliffs and buildings, we probably improve Δh_c from 16.8 to 835 mm [i.e., by 50 (= 10/0.2) times]. Furthermore, since $R_c \propto h_3$, R_c increases by 50 times and, thus, U^* [Eq. (4)] does not change. Moreover, since the cooling time t_0 is irrelevant to h_3, G decreases from 5.69 to $5.69/50 \simeq 0.114$ according to Eq. (6). Consequently, from Eq. (7), we obtain $\eta_B = \frac{1}{1+G} \sim 0.9$. Therefore, we expect that U_0 and Q improve by $0.9/0.15 \sim 6$ times; i.e., U_0 improves approximately from 1.2 to 7.2 mm/s, while Q improves approximately from 6 to 36 mm^3/s.

3. Diameter scale-up in the future

Since $R_c \propto d_2^{-4}$, diameter scale-up reduces R_c significantly. For example, if we increase d_2 from 2.5 to 5 mm, we probably improve R_c from 3.46 to 0.216 Pa s/mm^3 [i.e., by 2^{-4} times]. Consequently, from
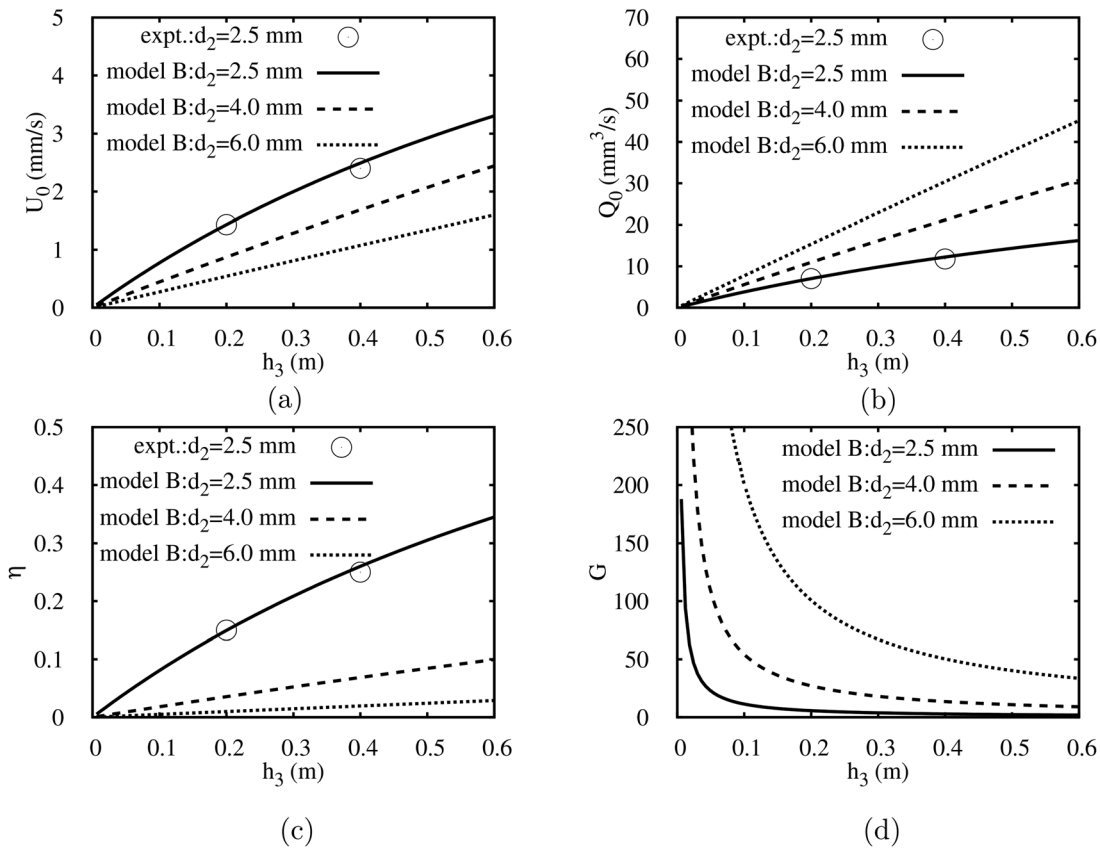

(a)

(b)

(c)

(d)

FIG. 11. Height scale-up ability in the range of $0 < h_3 \leq 0.6$ m (model B): (a) U_0 vs h_3, (b) Q_0 vs h_3, (c) η vs h_3, and (d) G vs h_3. Here, $I_p^* = 149.2$ W/m^2, $N_h = 10$, $\mu = 0.663$ Pa s, $\beta = 0.38 \times 10^{-3}$ 1/K, $\rho_0 = 992.3$ kg/m^3, $\alpha = 10$ W/(m^2 K), $C_p = 4.178$ kJ/(kg K), $C_1 = 1$, and $\Delta T = 22$ K; $l = 5\frac{h_3}{0.2}$ (m) and $d_1 = d_2 + 1.5$ (mm).

Eq. (4), U^* increases 16 times. Furthermore, from Eq. (6), G increases from 5.69 to $5.60 \times 16 \sim 91.04$ [by 16 times]; i.e., $G \gg 1$. In this case, from Eqs. (5) and (6), we obtain that $U_0 = \frac{1}{1+G} U^* \sim \frac{1}{G} U^* \sim \frac{h_3}{U^* t_0} U^* \sim \frac{h_3}{t_0} \sim 200/118.8 \sim 1.7$ mm/s. Therefore, we understand that there is a limit value ($h_3/t_0 \sim 1.7$ mm/s) for the expected flow velocity U_0 because of the auto flow adjustment effect explained in Secs. III B, III C, and IV A. In other words, U_0 and Q_0 do not become 16 times, even though R_c becomes 1/16 times.

4. Numerical analysis of scale-up ability

Figure 11 shows the numerical analysis using model B in Sec. IV A for the height scale-up ability in the range of $0 < h_3 \leq 0.6$ m. Here, $I_p^* = 149.2$ W/m^2, $N_h = 10$, $\mu = 0.663$ Pa s, $\beta = 0.38 \times 10^{-3}$ 1/K, $\rho_0 = 992.3$ kg/m^3, $\alpha = 10$ W/(m^2 K), $C_1 = 1$, $\Delta T = 22$ K, $l = 5\frac{h_3}{0.2}$ (m), and $d_1 = d_2 + 1.5$ (mm). As shown in Figs. 11(a) and 11(b), U_0 and Q_0 increase as h_3 increases. This is because η increases with h_3 [Fig. 11(c)] because of the rapid decreasing of G [Fig. 11(d)]. Furthermore, as shown in Figs. 11(a)–11(c), the values of the experimental results agree with the results of model B. In other words, the prediction of model B was supported by the experiment; i.e., by the additional experiment on the height scale-up problem (Fig. 8), we

demonstrated the height scale-up ability directly for the same structure. Thus, our prediction using model B is reliable.

Figure 12 shows the height scale-up ability in the range of $0 < h_3 \leq 10$ m at $d_2 = 2.5$, 4.0, and 6.0 mm. As shown in Figs. 12(a) and 12(b), we can expect that U_0 (Q_0) becomes approximately 8.5, 16, and 18 mm/s (40, 200, and 510 mm^3/s) at $d_2 = 2.5$, 4.0, and 6.0 mm, respectively. Here, since $d_2 = 6$ mm seems to be practical for the absorption of the light energy, the numerical analysis shows that the performance of our device can be improved at least up to the level that $U_0 \sim 18$ mm/s and $Q_0 \sim 510$ mm^3/s in the future. Moreover, we find that increasing rate of U_0 and Q_0 becomes small at the characteristic height $h_{3,c} \sim 2$ m for the curve at $d_2 = 2.5$ mm, while $h_{3,c}$ seems to become large as d_0 becomes large. This is because η approaches one at $d_2 = 2.5$ mm in the range $h_3 \geq 0.2$ m, as shown in Fig. 12(c). Furthermore, Fig. 12(d) shows the dependence of Δh_c on h_3 at $N_h = 10$ to 30. As shown in Fig. 12(d), we find that Δh_c increase with h_3 for all d_2. Note that Δh_c is a function of h_3, ΔT, and N_h; i.e., $\Delta h_c = \Delta h_c(h_3, \Delta T, N_h)$. In particular, since $\Delta h_c = 2.5$ m at $h_3 = 10$ m and $N_h = 30$, we understand that we can elevate water up to 10 m under the condition that $h_3 = 10$ m and $N_h = 30 \times 4 = 120$.

Figure 13 shows the diameter scale-up ability in the range of $0 < d_2 \leq 10$ mm. As shown in Fig. 13(a), U_0 has a peak at $d_2 \sim 1$–2 mm
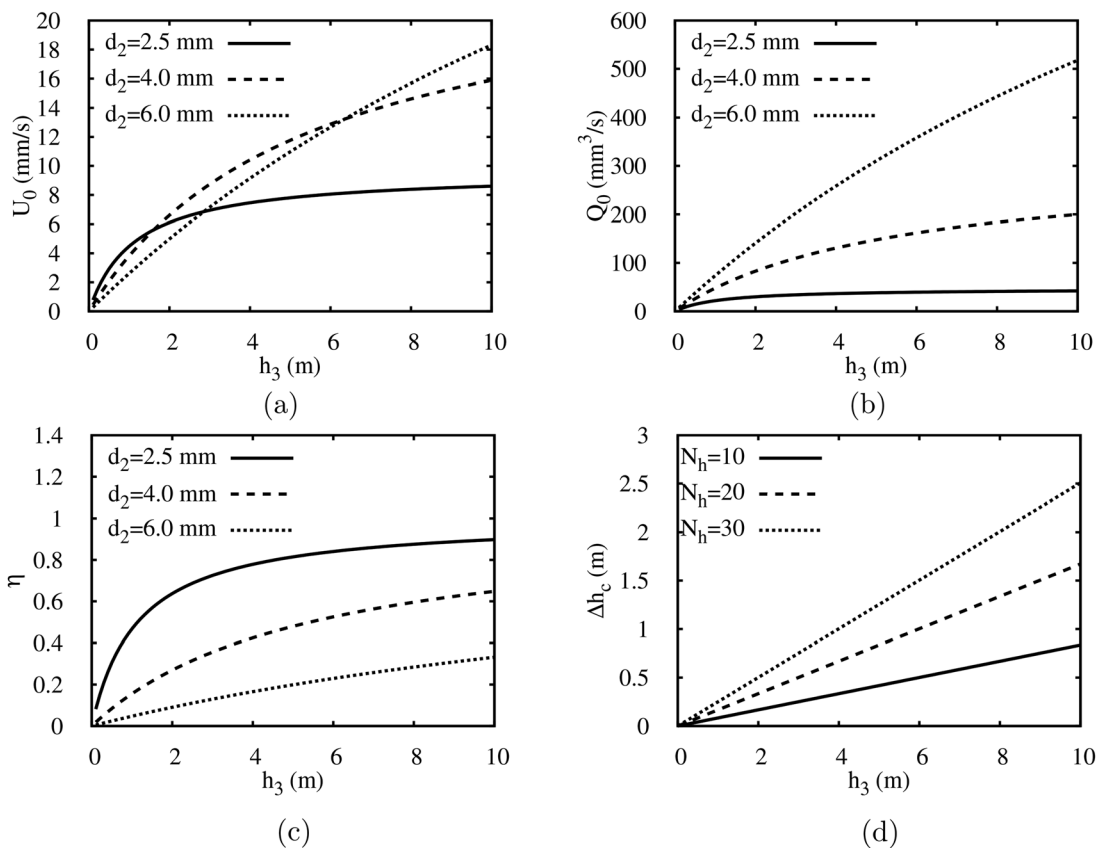

FIG. 12. Height scale-up ability in the range of $0 < h_3 \leq 10$ m (model B): (a) U_0 vs h_3 ($N_h = 10$), (b) Q_0 vs h_3 ($N_h = 10$), (c) η vs h_3 ($N_h = 10$), and (d) Δh_c vs h_3 (for all d_2). Here, $I_p^* = 149.2$ W/m^2, $\mu = 0.663$ Pa s, $\beta = 0.38 \times 10^{-3}$ 1/K, $\rho_0 = 992.3$ kg/m^3, $\alpha = 10$ W/(m^2 K), $C_p = 4.178$ kJ/(kg K), $C_1 = 1$, $\Delta T = 22$ K, $l = 5\frac{h_3}{0.2}$ (m), and $d_1 = d_2 + 1.5$ (mm).
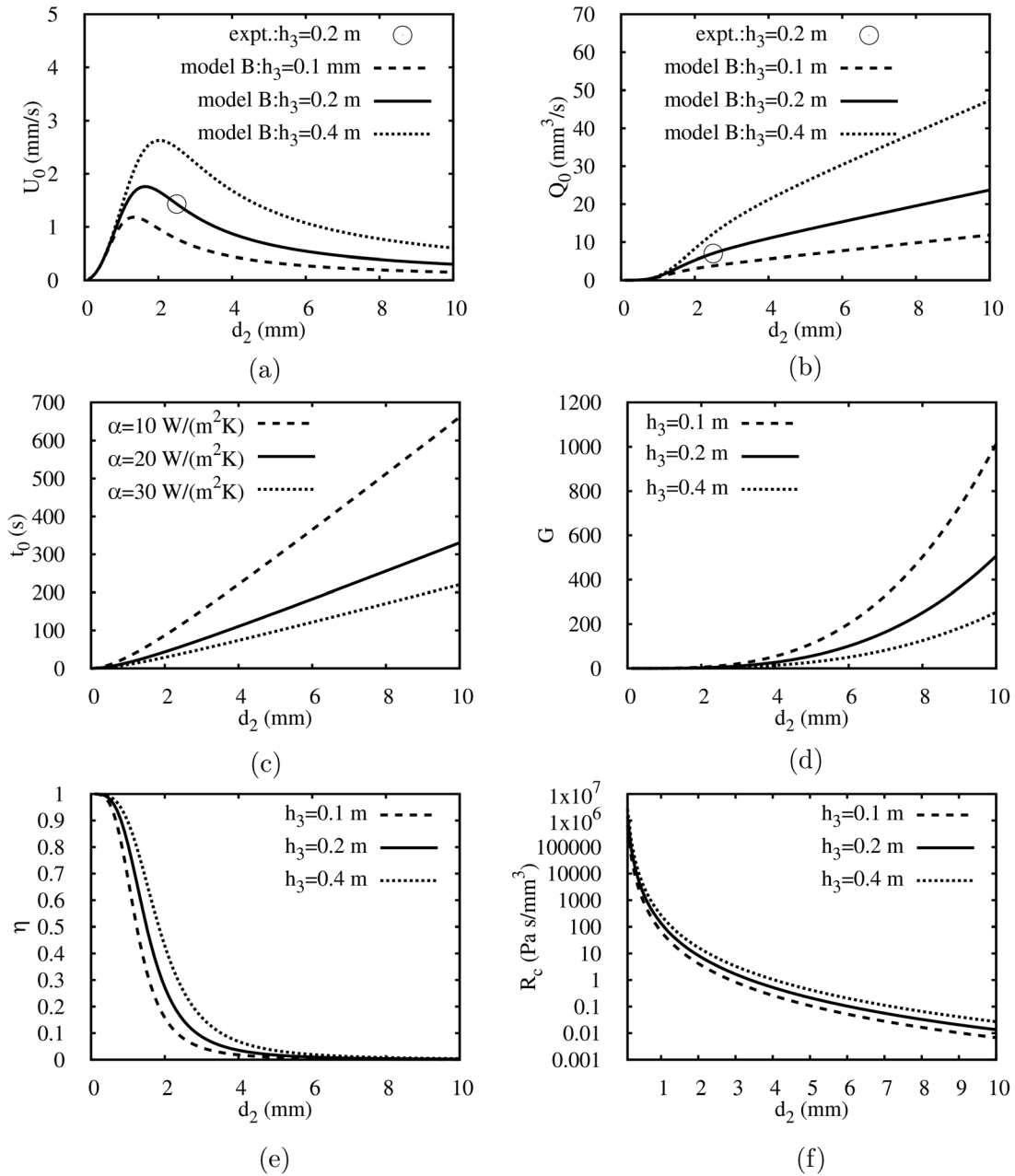
FIG. 13. Diameter scale-up ability (model B): (a) U_0 vs d_2 ($\alpha = 10$ W/m^2 K), (b) Q_0 vs d_2 ($\alpha = 10$ W/m^2 K), (c) t_0 vs d_2 (for all h_3), (d) G vs d_2 ($\alpha = 10$ W/m^2 K), (e) η vs d_2 ($\alpha = 10$ W/m^2 K), and (f) R_c vs d_2. Here, $I_p^* = 149.2$ W/m^2, $\mu = 0.663$ Pa s, $\beta = 0.38 \times 10^{-3}$ 1/K, $\rho_0 = 992.3$ kg/m^3, $\alpha = 10$ W/(m^2 K), $C_p = 4.178$ kJ/(kg K), $C_1 = 1$, and $\Delta T = 22$ K; $l = 5\frac{h_3}{0.2}$ (m), and $d_1 = d_2 + 1.5$ (mm).

and decreases with d_2 at $d_2 > 2$ mm, whereas Q_0 increases with d_2 as shown in Fig. 13(b). The reason why U_0 decreases with d_2 is that $t_0(d_2, \alpha)$ and $G(h_3, d_2, \Delta T, N_h) \equiv \frac{U^* t_0}{h_3}$ increase with d_2 [Figs. 13(c) and 13(d)] and, thus, $\eta(h_3, d_2, \Delta T, N_h, \alpha)$ decreases with d_2 [Fig. 13(e)]. Furthermore, since the cross-sectional area $S_0 = \pi(\frac{d_2}{2})^2$ increases with d_2, $Q_0 = U_0 S_0$ increases in Fig. 13(b). Note that since $R_c \propto d_2^{-4}$, R_c decreases rapidly with d_2 as shown in Fig. 13(f).

G. Difference from the previous light-driven BL pump

1. Proof of the water lift-up ability

Different from the current BL pump, the previous light-driven BL pump was examined in a circular fluidic channel.[24] Thus, there was no information on the water lift-up ability in the previous experiment. Therefore, we here proved the ability. In fact, since $\Delta P_{\text{expt.}}$ of the

previous BL pump was only 0.05 Pa, we can estimate that Δh_c $\sim \frac{\Delta P_{\text{expt.}}}{\rho_0 g} \sim 5.1\,\mu$m; i.e., it had no practical water lift-up ability. In other words, by the spiral tube design that includes the scale-up design discussed in Sec. IV F 1, we have first demonstrated that a light-driven BL pump can lift water from the source against the force of gravity, transport it horizontally, and push it out from the tube against surface tension. Specifically, we experimentally showed that the significant potential pressure difference ΔP_{theory} (= 162.6 Pa) enables the elevation of water of $\sim$5 mm (Fig. 5) from the source against the force of gravity ($\sim$50 Pa for $\Delta h = 5$ mm). Furthermore, the large pressure difference enables the removal of water from the spiral tube outlet against the Laplace pressure ΔP_γ (= 69.4 Pa) because of the surface tension. In addition, by the addition experiment in Fig. 6, we showed that our device worked at $\Delta h \sim 13$ mm.

2. Proof of the time persistence

Since the previous BL pump design uses a channel on a substrate,[24] there is a possibility that the temperature of the substrate gradually increases during the long-time irradiation and, thus, the pumping performance decreases. In addition, there is a possibility that the evaporation of water leads water channel to dry out and make its long-time operation difficult. In fact, we previously just reported the operation time of $\sim$60 s, although there was another reason that the tracer particles used to measure the flow velocity began to sink in $\sim$60 s.[24] In contrast, by the new design that spatially separates the sunny and shaded areas using a shading wall (corrugated cardboard with high thermal resistance), we have first proven that the light-driven BL pump works for a significant time (at least 55 min in Fig. 4) with a performance of $U \sim 1.2$ mm/s, $Q \sim 6$ mm^3/s, and $\Delta P \sim 20$ Pa [under an illumination condition of $I_p = 37\,300$ lx ($I_p^* = 149.2$ W/ m^2)]. In other words, we have shown that a design that maintains a stable periodic local temperature distribution is feasible in a light-driven BL pump. In addition, by the addition experiment in Fig. 6, we showed that our device worked at least for 3 h.

3. Direct measurement of the temperature distribution and the new BL-pump design concept

Different from the previous study,[24] the current study using a spiral tube structure enables the direct measurement of the time evolution of the periodic local temperature distribution using the thermography (see Fig. 3). Consequently, we were able to observe a clear transportation of the heat energy from the sunny side to the shadow side along with the steady temperature distribution (at $t \geq 462$ s in Fig. 3). Based on this observation, we succeeded in explaining the existence of the initial peak of U and the adjustment phenomenon to the steady state (described by model B). In other words, through the current BL-pump study, we have obtained the new BL-pump design concept that Eq. (4), which gives the maximum achievable potential velocity U^*, is modified to Eq. (5) by the effect of the transport of heat energy from the hot region to the cold region by flow generation. Here, to approach U to the ideal velocity U^*, we need to realize ideal heat dissipation such that heat transportation length l_0 in Sec. IV A approaches zero.

H. Difference from the synthetic trees

1. Difficulty in pumping water up to a certain height and taking it out

A hydrophilic vertical tube of diameter d_2 and surface tension γ has an ability to lift water, and it is well known as a pumping mechanism of trees.[27,28] In detail, from the balance equation between the gravity force $\pi(\frac{d_2}{2})^2 \Delta h \rho_0 g$ and the surface tension $\pi d_2 \gamma$, we can derive the pumping height Δh as $\Delta h \simeq \frac{4\gamma}{\rho_0 g d_2}$; e.g., $\Delta h = 11.4$ mm if $d_2 = 2.5$ mm. However, to take the water from the height position, we need to move the water at least against a gravity force $\pi(\frac{d_2}{2})^2 h \rho_0 g$. Thus, if we move it by the velocity U, the mechanical work $\pi(\frac{d_2}{2})^2 h \rho_0 g U$ (= $\dot{m} g h$) is required per a second at least, and it tells us the energy conservation law; i.e., water will not continue to move from a low to a high place without an external supply of energy. Nevertheless, natural trees can continue to pump water up to a high press, and the key strategy is considered to be the transpiration of water from the surface.[27,28] Obviously, the externally supplied energy is the thermal energy due to the sunlight. In detail, the pumping mechanism of trees is usually explained by the cohesion-tension theory, i.e., loss of water by evaporation reduces the pressure of the liquid water in the leaf; then, this reduced pressure pulls liquid water.[29]

2. Studies of synthetic trees

Studies of synthetic trees that mimic natural trees have been attracting much attention.[27–37] For example, in 2008, Wheeler and Stroock[29] presented the design and operation of a microfluidic system using a synthetic hydrogel as a synthetic tree, which shows continuous extraction of water from the source (mass flow rate: $\sim$14 μg/s). In 2019, Agrawal et al.[36] demonstrated a significant increase in the fluid flow rate by using a synthetic tree consisting of a microporous membrane integrated with a branched, fractal channel network ($Q \sim 0.1$ mm^3/s), while Shi et al.[35] reported self-stabilizing transpiration in synthetic leaves. In 2021, Eyegheleme et al.[28] reported that the synthetic tree harvested approximately three times condensed water (e.g., $\sim$0.27 kg/m^2 h at $I_p^* \sim 433$ W/m^2) than an equivalent bulk reservoir, while Eyegheleme et al.[27] reported a comprehensive theoretical model of transpiration for synthetic trees comprised of vertically oriented tube array connected at the top a nanoporous synthetic leaf in 2022.

3. Difference from the synthetic trees

Different from the synthetic trees that use transpiration,[27–37] our light-driven BL pump uses a buoyancy force due to the temperature difference ΔT that is produced by the sunlight. In other words, the synthetic tree requires a large evaporation latent heat ($h_e \simeq 2250$ kJ/ kg), whereas our BL pump uses a relatively small sensible heat ($C_p \Delta T \sim 92$ kJ/kg). Therefore, our BL pump seems to have an advantage in the consumption of energy. In fact, since the total irradiation area S_t of our device is $\sim$0.01 m^2 ($\sim W_1 h_3$) and $\sim$6 mm^3/s corresponds to 21.6 g/h, our device (Fig. 4) produces $\sim$2.16 kg/m^2 h at $I_p^* = 149.2$ W/m^2. Although a simple comparison cannot be made, the pumping performance of our device is approximately 23.2 (= $\frac{2.16}{0.27}\frac{433}{149.2}$) times larger than that of Eyegheleme et al.'s device for the same irradiation intensity, because Eyegheleme et al.'s device produces

$\sim$0.27 kg/m^2 h at $I_p^* \sim$ 433 W/m^2.[28] In other words, although the studies of synthetic trees are very challenging, our light-driven BL pump seems to be more practical than the synthetic tree in the point of a pumping rate. In addition, as discussed in Sec. IV F, since our BL pump has a large design margin, there is a possibility that we can improve the pumping performance dramatically in the future. Therefore, our device seems to be promising at least compared to the synthetic trees.

4. About the other studies on pushing water out of tube

There are many studies on pushing water out of tube against the surface tension. For example, Nazari et al.[38] reported the comparison of formation of Newtonian and non-Newtonian drops in air using image processing. Wang et al.[39] reported the regimes and dynamics of droplet formation during ejection from a vertical capillary nozzle. Borthakur et al.[40] reported numerical investigation on the dynamics of drop formation from submerged orifices under the influence of an external electric field. Wagoner et al.[41] proposed a new way of determining axial scaling during capillary pinch-off process. Liu and Derby[42] reported a parameter space that determine the printability of a fluid for a inkjet device. The knowledge of these studies probably useful when we consider how water is pushed out of tube in detail, although it is beyond the scope of this study.

I. Difference from natural circulation loops and solar stills

Natural circulation (NC) loop is well known as a pump using convection phenomenon especially in the nuclear power field.[43–47] For example, Rai et al.[43] reported mathematical and numerical analysis for the existence of dynamic instability phenomena in a rectangular shape of natural circulation loop at supercritical condition using supercritical water as a working fluid, while Thippeswamy and Yadav[44] reported the heat transfer enhancement using CO_2 in a NC loop. Furthermore, Guo et al.[45] reported a code based on the homogeneous equilibrium model for two-phase flow (consisting of liquid and vapor) to simulate the transient behavior of the open natural circulation (ONC) system,

while Yan et al.[46] experimentally reported geysering phenomenon in a two-phase ONC. Here, ONC systems often mean the NC systems that can release the steam into the environment and can return the liquid for the recirculation, to dissipate heat, and often to cool the nuclear reactor.[45] Furthermore, as a device using a sunlight, Jinshah et al.[47] reported an ONC using a parabolic sunlight collector. Although these studies on NC loops are challenging, they usually consider a single loop and usually do not consider water extraction from tubes.[43–47]

Solar still is a device that produces drinking water by evaporating liquid water into a vapor and condensed it into liquid water with a transparent lid along with sunlight.[48,49] For example, Rahmani et al.[48] reported the negative effect of the effect of the external condenser on the conventional solar still performance, while Rahmani and Zaidi[49] reported the effect of condenser design on the performance of the solar still having a NC loop function and reported that the maximum hourly freshwater production is 0.371, 0.428, and 0.542 kg/m^2 h for the single-tube, finned-tube, and three-tube condensers, respectively, under typical summer condition ($I_p^* \sim$ 1 kW/m^2). Here, a condenser is a heat exchanger used to condense vapor water to liquid water and leads to the enhancement of evaporation and condensation rates in solar still.[49] Although a simple comparison cannot be made, the performance of the device is approximately 27 ($\sim \frac{2.16}{0.542}\frac{1000}{149.2}$) to 39 ($\sim \frac{2.16}{0.371}\frac{1000}{149.2}$) times larger than that of the solar still,[49] since our device produces water of $\sim$2.16 kg/m^2 h under $I_p^* =$ 149.2 W/m^2 (see Sec. IV H 3). In other words, although the technology of solar stills is in a practical level, our light-driven BL pump seems to be more practical than the solar stills in the point of a water production rate. In addition, there is a large design margin for our device, as discussed in Sec. IV F. Therefore, we consider that our device is promising in the future.

J. Practical usage and utility of the proposed technique

Figures 14(a) and 14(b) show the dependence of Q and U on Δh, respectively, for the practical usage. Here, $I_p^* =$ 149.2 W/m^2, $N_h =$ 240, and $h_3 =$ 10 m, i.e., we consider the BL pump having an ability that $\Delta h_c \sim$ 20 m. From these figures, we find that if we use this pump under the condition $\Delta h =$ 10 m, we can obtain the water of

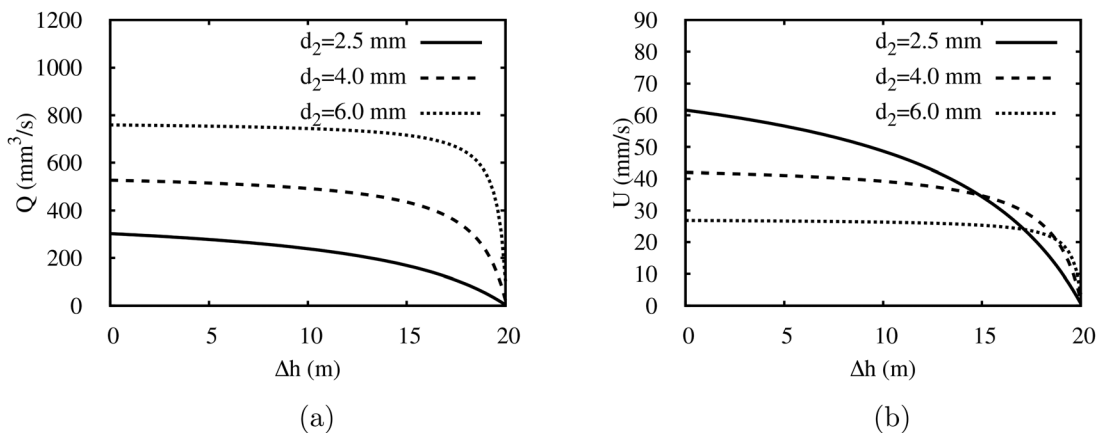**FIG. 14.** Dependence of Q and U on Δh for the practical usage (model B): (a) Q vs Δh and (b) U vs Δh. Here, $I_p^* =$ 149.2 W/m^2, $N_h =$ 240, $h_3 =$ 10 m, $\mu =$ 0.663 Pa s, $\beta = 0.38 \times 10^{-3}$ 1/K, $\rho_0 =$ 992.3 kg/m^3, $\alpha =$ 10 W/(m^2 K), $C_p =$ 4.178 kJ/(kg K), $C_1 =$ 1, and $\Delta T =$ 22 K; $l = 5\frac{h_3}{0.2}$ (m) and $d_1 = d_2 +$ 1.5 (mm).
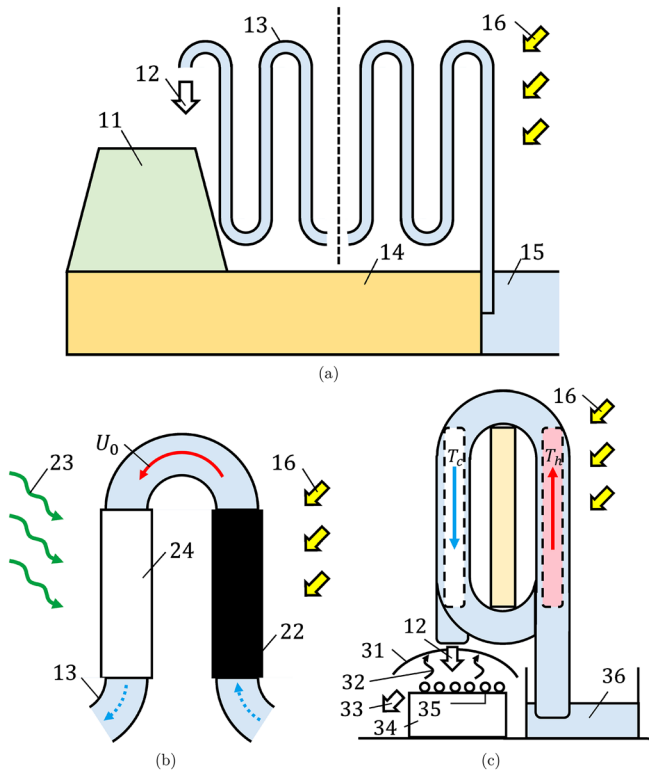
FIG. 15. Practical usage of the proposal technique: (a) pumping water to a high place, (b) improvement of light absorption and heat dissipation, and (c) fresh water and salt production from the sea water. 11: high place, 12: transported water, 13: tube having a spiral or zig–zag structure, 14: land, 15: water source, 16: sunlight, 22: light absorption black tube, 23: wind, 24: light reflected aluminum tube (or light shaded tube), 31: transparent lid, 32: vapor, 33: fresh water, 34: iron plate, 35: salt, and 36: sea water.

$Q \simeq 239$, 493, and 744 mm^3/s ($U \simeq 49$, 39, and 26 mm/s) at $d_2 = 2.5$, 4.0, and 6.0 mm, respectively. In other words, by using the BL pump of $d_2 = 6$ mm, $N_h = 240$, and $h_3 = 10$ m under the sunlight of $I_p^* = 149.2$ W/m^2, we can use the water of ∼2.7 l per hour at the high place of 10 m above the water source. Furthermore, since the typical irradiation intensity $I_p^{*,sun}$ of sun is 1 kW/m^2, we can expect more water on sunny days. In addition, our device has a lot of design margin. Therefore, our device is promising at least for the personal use, although we may need to overcome the cost problem in the future.

Figure 15 shows the practical usage of the proposal technique. Therefore, as shown in Fig. 15(a), we can pump up water from a water source to a high place (e.g., $\Delta h = 10$ m) by using an above-mentioned pump ($d_2 = 6$ mm, $h_3 = 10$ m, and $N_h = 240$) with a tube having a spiral or zig-zag structure. Furthermore, as shown in Fig. 15(b), we may improve a light absorbing rate by using a light absorbing black tube for the sunny side, whereas we may improve a dissipation ability by using a light reflected aluminum tube (or light shaded tube) with heat dissipation fins. Moreover, as shown in Fig. 15(c), we may produce drinking water along with salt by using our BL pump with an iron plate which has a transparent lid above it. In addition, since the spiral tube design enables the use of ordinary vinyl tubes as a light-driven BL pump, our technology may help a wide range of people if

we can propose a personal usage with an ultra-low cost; e.g., one may develop a practical machine for the personal use by the do-it-yourself carpenter work. In the future, we would like to realize these plans.

V. CONCLUSION

In conclusion, we have demonstrated that a light-driven BL water pump with a spiral tube structure can lift water against the force of gravity, transport it horizontally, and remove it from the tube against surface tension. Our technology should help achieve sustainable transportation of water.

AUTHOR DECLARATIONS
Conflict of Interest

The authors have no conflicts to disclose.

Author Contributions

Hideyuki Sugioka: Conceptualization (lead); Data curation (supporting); Formal analysis (supporting); Funding acquisition (lead); Methodology (equal); Project administration (lead); Resources (lead); Software (supporting); Supervision (lead); Visualization (equal); Writing – original draft (lead); Writing – review & editing (lead). **Hiroki Yoshijima:** Data curation (lead); Formal analysis (lead); Investigation (lead); Methodology (equal); Software (lead); Visualization (equal).

DATA AVAILABILITY

The data that support the findings of this study are available within the article.

REFERENCES

[1]C. He, Z. Liu, J. Wu, X. Pan, Z. Fang, J. Li, and B. A. Bryan, "Future global urban water scarcity and potential solutions," Nat. Commun. **12**, 4667 (2021).

[2]N. Zehtabiyan-Rezaie, N. Alvandifar, F. Saffaraval, M. Makkiabadi, N. Rahmati, and M. Saffar-Avval, "A solar-powered solution for water shortage problem in arid and semi-arid regions in coastal countries," Sustainable Energy Technol. Assess. **35**, 1–11 (2019).

[3]S. M. Wazed, B. R. Hughes, D. O'Connor, and J. Kaiser Calautit, "A review of sustainable solar irrigation systems for Sub-Saharan Africa," Renewable Sustainable Energy Rev. **81**, 1206 (2018).

[4]R. Yan, T. S. McClure, I. H. Jasim, A. K. R. Koppula, S. Wang, M. Almasri, and C.-L. Chen, "Enhanced water capture induced with electrowetting-on-dielectric (EWOD) approach," Appl. Phys. Lett. **113**, 204101 (2018).

[5]Y. Jiang, S. Savarirayan, Y. Yao, and K.-C. Park, "Fog collection on a superhydrophilic wire," Appl. Phys. Lett. **114**, 083701 (2019).

[6]J. Li, R. Ran, H. Wang, Y. Wang, Y. Chen, S. Niu, P. E. Arratia, and S. Yang, "Aerodynamics-assisted, efficient and scalable kirigami fog collectors," Nat. Commun. **12**, 5484 (2021).

[7]Z. Song, E. S. Lin, M. H. Uddin, H. A. Abid, J. W. Ong, O. W. Liew, and T. W. Ng, "Fog harvesting with highly wetting and nonwetting vertical strips," Langmuir **38**, 1845 (2022).

[8]K. Yin, Z. Wu, J. Wu, Z. Zhu, F. Zhang, and J.-A. Duan, "Solar-driven thermal-wind synergistic effect on laser-textured superhydrophilic copper foam architectures for ultrahigh efficient vapor generation," Appl. Phys. Lett. **118**, 211905 (2021).

[9]X. Zhou, F. Zhao, P. Zhang, and G. Yu, "Solar water evaporation toward water purification and beyond," ACS Mater. Lett. **3**, 1112 (2021).

19 July 2024 06:29:46

[10]L. F. Greenlee, D. F. Lawler, B. D. Freeman, B. Marrot, and P. Moulin, "Reverse osmosis desalination: Water sources, technology, and today's challenges," Water Res. **43**, 2317 (2009).

[11]L. Wang, Y. Feng, K. Wang, and G. Liu, "Solar water sterilization enabled by photothermal nanomaterials," Nano Energy **87**, 106158 (2021).

[12]X. Zhu, V. Mathai, R. J. A. M. Stevens, R. Verzicco, and D. Lohse, "Transition to the ultimate regime in two-dimensional Rayleigh-Bénard convection," Phys. Rev. Lett. **120**, 144502 (2018).

[13]V. Bouillaut, S. Lepot, S. AumaÝtre, and B. Gallet, "Transition to the ultimate regime in a radiatively driven convection experiment," J. Fluid Mech. **861**, R5 (2019).

[14]Q. Wang, R. Verzicco, D. Lohse, and O. Shishkina, "Multiple states in turbulent large-aspect-ratio thermal convection: What determines the number of convection rolls?," Phys. Rev. Lett. **125**, 074501 (2020).

[15]R. Yang, K. L. Chong, Q. Wang, R. Verzicco, O. Shishkina, and D. Lohse, "Periodically modulated thermal convection," Phys. Rev. Lett. **125**, 154502 (2020).

[16]P. Urban, P. Hanzelka, T. Králik, V. Musilová, and L. Skrbek, "Thermal waves and heat transfer efficiency enhancement in harmonically modulated turbulent thermal convection," Phys. Rev. Lett. **128**, 134502 (2022).

[17]R. E. Ecke, X. Zhang, and O. Shishkina, "Connecting wall modes and boundary zonal flows in rotating Rayleigh-Bénard convection," Phys. Rev. Fluids **7**, L011501 (2022).

[18]X.-Q. Guo, B.-F. Wang, J.-Z. Wu, K. L. Chong, and Q. Zhou, "Turbulent vertical convection under vertical vibration," Phys. Fluids **34**, 055106 (2022).

[19]S. Bhattacharya, M. K. Verma, and A. Bhattacharya, "Predictions of Reynolds and Nusselt numbers in turbulent convection using machine-learning models," Phys. Fluids **34**, 025102 (2022).

[20]D.-L. Dong, B.-F. Wang, Y.-H. Dong, Y.-X. Huang, N. Jiang, Y.-L. Liu, Z.-M. Lu, X. Qiu, Z.-Q. Tang, and Q. Zhou, "Influence of spatial arrangements of roughness elements on turbulent Rayleigh-Bénard convection," Phys. Fluids **32**, 045114 (2020).

[21]J. Zhang, S. Yao, F. Fei, M. Ghalambaz, and D. Wen, "Competition of natural convection and thermal creep in a square enclosure," Phys. Fluids **32**, 102001 (2020).

[22]H. Sugioka and Y. Someya, "Natural circulation pump with asymmetrical heat transfer wall as the element of Büttiker–Landauer thermal ratchet," Phys. Fluids **32**, 112016 (2020).

[23]H. Sugioka and Y. Someya, "Rapid increase in strength of vortices and a directional net flow due to Marangoni force in Büttiker–Landauer ratchet," Phys. Fluids **34**, 064113 (2022).

[24]H. Sugioka, S. Hatanaka, and Y. Someya, "Sustainable light-driven water pump using Büttiker–Landauer ratchet," Appl. Phys. Lett. **120**, 123901 (2022).

[25]R. Benjamin and R. Kawai, "Inertial effects in Büttiker-Landauer motor and refrigerator at the overdamped limit," Phys. Rev. E **77**, 051132 (2008).

[26]R. W. Thimijan and R. D. Heins, "Photometric, radiometric, and quantum light units of measure: A review of procedures for interconversion," HortScience **18**, 818 (1983).

[27]N. L. Eyegheleme, K. Peng, and J. B. Boreyko, "Modeling transpiration in synthetic trees," Int. J. Heat Mass Transfer **183**, 122121 (2022).

[28]N. L. Eyegheleme, W. Shi, L. H. De Koninck, J. L. O'Brien, and J. B. Boreyko, "Synthetic trees for enhanced solar evaporation and water harvesting," Appl. Phys. Lett. **118**, 251601 (2021).

[29]T. D. Wheeler and A. D. Stroock, "The transpiration of water at negative pressures in a synthetic tree," Nature **455**, 208 (2008).

[30]X. Noblin, L. Mahadevan, I. A. Coomaraswamy, D. A. Weitz, N. M. Holbrook, and M. A. Zwieniecki, "Optimal vein density in artificial and real leaves," Proc. Natl. Acad. Sci. U.S.A. **105**, 9140 (2008).

[31]O. Vincent, D. A. Sessoms, E. J. Huber, J. Guioth, and A. D. Stroock, "Drying by cavitation and poroelastic relaxations in porous media with macroscopic pores connected by nanoscale throats," Phys. Rev. Lett. **113**, 134501 (2014).

[32]O. Vincent, A. Szenicer, and A. D. Stroock, "Capillarity-driven flows at the continuum limit," Soft Matter **12**, 6656 (2016).

[33]M. Lee, H. Lim, and J. Lee, "Fabrication of artificial leaf to develop fluid pump driven by surface tension and evaporation," Sci. Rep. **7**, 14735 (2017).

[34]Z. Lu, K. L. Wilke, D. J. Preston, I. Kinefuchi, E. Chang-Davidson, and E. N. Wang, "An ultrathin nanoporous membrane evaporator," Nano Lett. **17**, 6217 (2017).

[35]W. Shi, J. R. Vieitez, A. S. Berrier, M. W. Roseveare, D. A. Surinach, B. R. Srijanto, C. P. Collier, and J. B. Boreyko, "Self-stabilizing transpiration in synthetic leaves," ACS Appl. Mater. Interfaces **11**, 13768 (2019).

[36]P. Agrawal, P. S. Gandhi, M. Majumder, and P. Kumar, "Insight into the design and fabrication of a leaf-mimicking micropump," Phys. Rev. Appl. **12**, 031002 (2019).

[37]W. Shi, R. M. Dalrymple, C. J. McKenny, D. S. Morrow, Z. T. Rashed, D. A. Surinach, and J. B. Boreyko, "Passive water ascent in a tall, scalable synthetic tree," Sci. Rep. **10**, 230 (2020).

[38]A. Nazari, A. Zadkazemi Derakhshi, A. Nazari, and B. Firoozabadi, "Drop formation from a capillary tube: Comparison of different bulk fluid on Newtonian drops and formation of Newtonian and non-Newtonian drops in air using image processing," Int. J. Heat Mass Transfer **124**, 912 (2018).

[39]Z. Wang, Y. Zhang, R. Li, Q. Wang, and J. Wang, "An experimental study on drop formation from a capillary tube," J. Braz. Soc. Mech. Sci. Eng. **42**, 110 (2020).

[40]M. P. Borthakur, G. Biswas, and D. Bandyopadhyay, "Dynamics of drop formation from submerged orifices under the influence of electric field," Phys. Fluids **30**, 122104 (2018).

[41]B. W. Wagoner, S. S. Thete, and O. A. Basaran, "A new experimental method based on volume measurement for determining axial scaling during breakup of drops and liquid threads," Phys. Fluids **30**, 082102 (2018).

[42]Y. Liu and B. Derby, "Experimental study of the parameters for stable drop-on-demand inkjet performance," Phys. Fluids **31**, 032004 (2019).

[43]S. Kumar Rai, P. Kumar, and V. Panwar, "Mathematical and numerical investigation of Ledinegg flow excursion and dynamic instability of natural circulation loop at supercritical condition," Ann. Nucl. Energy **155**, 108129 (2021).

[44]L. R. Thippeswamy and A. Kumar Yadav, "Heat transfer enhancement using CO_2 in a natural circulation loop," Sci. Rep. **10**, 1507 (2020).

[45]X. Guo, Z. Sun, J. Wang, S. Yu, and L. Gao, "Numerical simulation of the transient behaviors in an open natural circulation system with a large scale," Ann. Nucl. Energy **77**, 83 (2015).

[46]X. Yan, G. Fan, and Z. Sun, "Study on flow characteristics in an open two-phase natural circulation loop," Ann. Nucl. Energy **104**, 291 (2017).

[47]B. Jinshah, K. Balasubramanian, R. Kottala, and S. Divakar, "Influence of power step on the behavior of an Open Natural Circulation Loop as applied to a parabolic trough collector," Renewable Energy **181**, 1046 (2022).

[48]A. Rahmani, F. Khemmar, and Z. Saadi, "Experimental investigation on the negative effect of the external condenser on the conventional solar still performance," Desalination **501**, 114914 (2021).

[49]A. Rahmani and Y. Zaidi, "Effect of condenser design on the performance of the natural circulation loop solar still: An experimental study," Heat Transfer **51**, 4783 (2022).

19 July 2024 06:29:46